PLIOCENE EXHUMATION OF THE TRUMSING LA AREA (EASTERN HIMALAYA, KINGDOM OF BHUTAN) USING U-TH-SM/HE THERMOCHRONOLOGY

Kyle Landry

Submitted in Partial Fulfillment of the Requirements

for the Degree of Bachelor of Sciences, Honours

Department of Earth Sciences

Dalhousie University, Halifax, Nova Scotia

March 14, 2010

DALHOUSIE UNIVERSITY
Inspiring Minds

Department of Earth Sciences
Halifax, Nova Scotia
Canada B3H 4J1
(902) 494-2358
FAX (902) 494-6889

DATE: April 26, 2010

AUTHOR: Kyle Landry

TITLE: Pliocene Exhumation of the Trumsing La Area (Eastern Himalaya, Kingdom of Bhutan) Using U-Th-Sm/He Thermochronology

Degree: BSc Honours Convocation: May Year: 2010

Permission is herewith granted to Dalhousie University to circulate and to have copied for non-commercial purposes, at its discretion, the above title upon the request of individuals or institutions.

Signature of Author

Abstract

The ongoing convergence between India and Eurasia since continent-continent collision occurred ~ 55 My ago, formed the Himalayan orogen, the highest mountain range on Earth. Remarkably continuous tectonostratigraphic units and structures along strike characterize its 2000 km-long range front. The topographic uplift of the range induced perturbations of atmospheric circulations patterns sometime between ~20-35 Ma and led to the establishment of the Indian Summer Monsoon (ISM) along the southern flank of the Himalaya. The monsoon is responsible for about 80% of the annual rainfall along the range front and results from the condensation of wet air derived from the Bay of Bengal to the South and travelling northward before being blocked by the Himalayan Mountains. Consequently, strong interactions between tectonic and climatic processes have likely conditioned the exhumational and landscape evolution of the range in the Late Tertiary. Furthermore, the only raised topography outboard the Himalayan range front, the Shillong plateau, is located south of Bhutan on the ISM trajectory and was uplifted in the Pliocene. The Shillong plateau concentrates 30-40% of monsoonal rainfall along its southern slope and consequently central and eastern Bhutan receives about half of the rainfall as the Sikkim Himalaya situated further west. The objective of this study is to quantify Late Tertiary potential changes of exhumation rate in the Trumsing La area (central Bhutan) located in the rain shadow of the Shillong plateau. Four bedrock samples collected along a vertical profile have been dated using (U-Th-Sm)/He thermochronology on apatite crystals (AHe). The effective closure temperature of this thermochronometric system is about 75 °C and helps to derive exhumation rates of the upper 1-2 km of the crust. Published apatite fission-track results, a method providing information on the exhumation of deeper crustal levels (closure temperature is 120 °C), obtained from the same samples yielded an exhumation rate of 0.6 mm/yr in the Late Miocene. The AHe results yielded an exhumation rate of 1.9mm/yr at the Miocene-Pliocene boundary. Despite the limitations of the experiment, such as the sensitivity of the AHe system to advection of shallow isotherms due to topographic changes, our results help define exhumation rates at the Miocene-Pliocene boundary. Along with numerical data, the major limitations of our experiment have given us information on how to refine our sampling strategy for future experiments so that if this study is repeated, a denser sample interval can be taken, along with a larger number of grains per sample.

Keywords: Apatite, AHe, Thermochronology, age-elevation profile, exhumation rate, Trumsing La, Bhutan, Shillong Plateau

Acknowledgements

I would like to thank my supervisor Dr. Isabelle Coutand for her immense help throughout this entire project: collection, processing of samples and collection of apatites and reading and re-reading my chapter drafts while giving me timely and useful feedback. Collaborator Maria Giuditta Fellin from ETH Zurich, Switzerland for her analysis of our samples for parent isotopes and her information on the methods for using the ICP-MS and sample preparation. Keith Taylor from the noble gas extraction lab at Dalhousie University for processing our samples for He analysis. Also, Dr. Pat Ryall for his corrections of my chapters. Finally, Konstanza Stubner for teaching me how to use the sampling microscope, how to properly pick grains and for answering any questions I may have had.

Table of Contents

Section Titles

Chapter 1: Introduction, Geology, Morphology and Expected Results

This chapter will include an in-depth description of the overall Himalayan geology, Bhutanese geology, a geomorphological comparison of range-fronts, rainfall distribution in the Himalayas and the expected results of this study.

1.1 Introduction

The convergence between the Indian and Eurasian lithospheric plates resulting in continent-continent collision ~50 Ma ago induced the uplift of the Himalayas, the highest mountain range on Earth (Patriat and Achache, 1984). The range front of the Himalayas is characterized by ~2000 km of fairly continuous tectonic and stratigraphic features along the strike of the orogen (Fig. 1.1). The physical barrier created by the range has a profound effect on the local climate by forcing moist winds derived from the Indian Ocean to condense and deliver heavy and localized rainfalls along its southern rampart; this phenomenon is known as the Indian Summer Monsoon. Some studies have placed the establishment of the monsoon between 20 and 35 Ma, (e.g. Harris, 2006) although this timing still remains imprecise and controversial. Tectonic and climatic processes closely interplay to shape the modern landscape and their contribution to the erosion of the upper part of the continental crust (or to upper crustal exhumation) remains a matter of debate. This study focuses on the Eastern Himalaya in the Trumsing La area (eastern Bhutan); The Kingdom of Bhutan is surrounded by India on the southern, eastern and western sides and by Tibet in the North (Fig. 1.2). This segment of the orogen is of particular interest because it is located in the lee of the only raised topography existing in the foreland of the Himalayan front, the Shillong plateau (Grujic et al., 2006). The Pliocene uplift of the plateau has likely perturbed the distribution of the Indian Summer

Monsoon (ISM) rainfalls by concentrating 30-40% of the seasonal monsoon precipitation on its southern slope and creating a rain shadow on the southern rampart of the Eastern Bhutan Himalaya (Grujic et al., 2006; Biswas et al., 2007). The purpose of this study is to quantify Late Tertiary potential changes in upper crustal exhumation rate (equivalent to erosion rates in orogenic setting) in the Trumsing La area located in the rain shadow of the Shillong plateau. Four bedrock samples collected along a vertical profile have been dated using (U-Th-Sm)/He thermochronology on apatite crystals (AHe) to derive exhumation rates for the upper 1-2 km of the continental crust for the latest Tertiary period of time. Using these exhumation rates we will explore the possibility of a change in exhumation rates in the Late Tertiary and speculate on possible origins of this change.

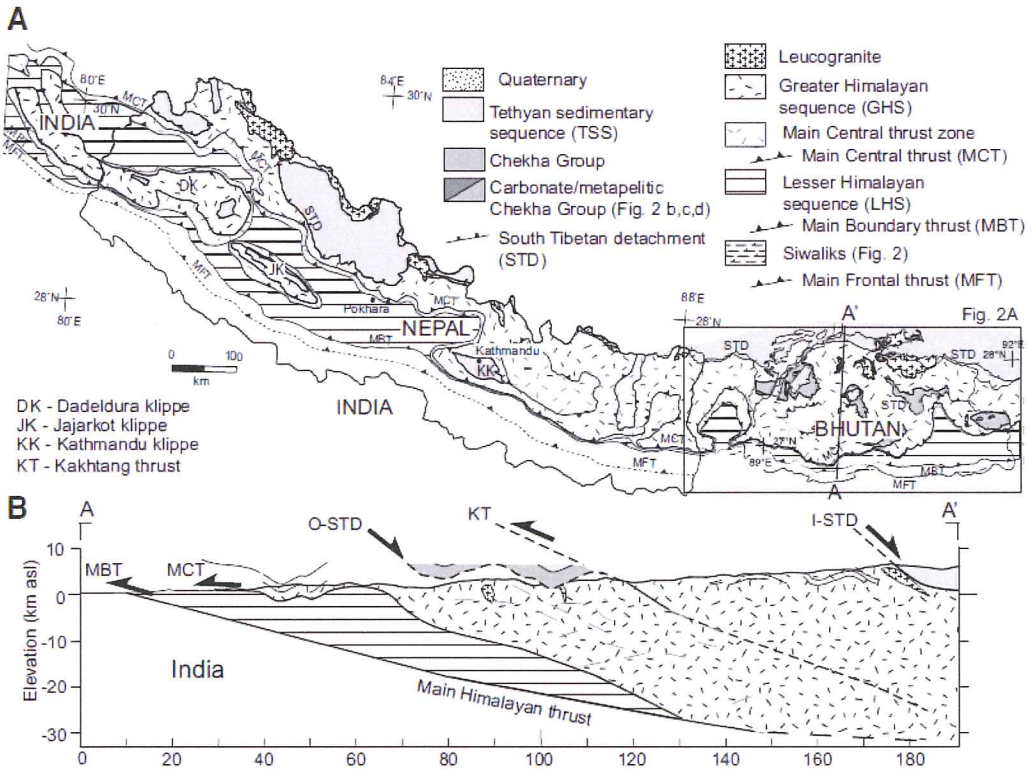

Figure 1.1: A) Map of the Himalayan orogen modified from McQuarrie et al. (2008). B) Generalized cross section through 90°E showing the main structures of the eastern Himalaya based on the geological map by Gansser (1983). Both figures are from Kellett et al., 2009.

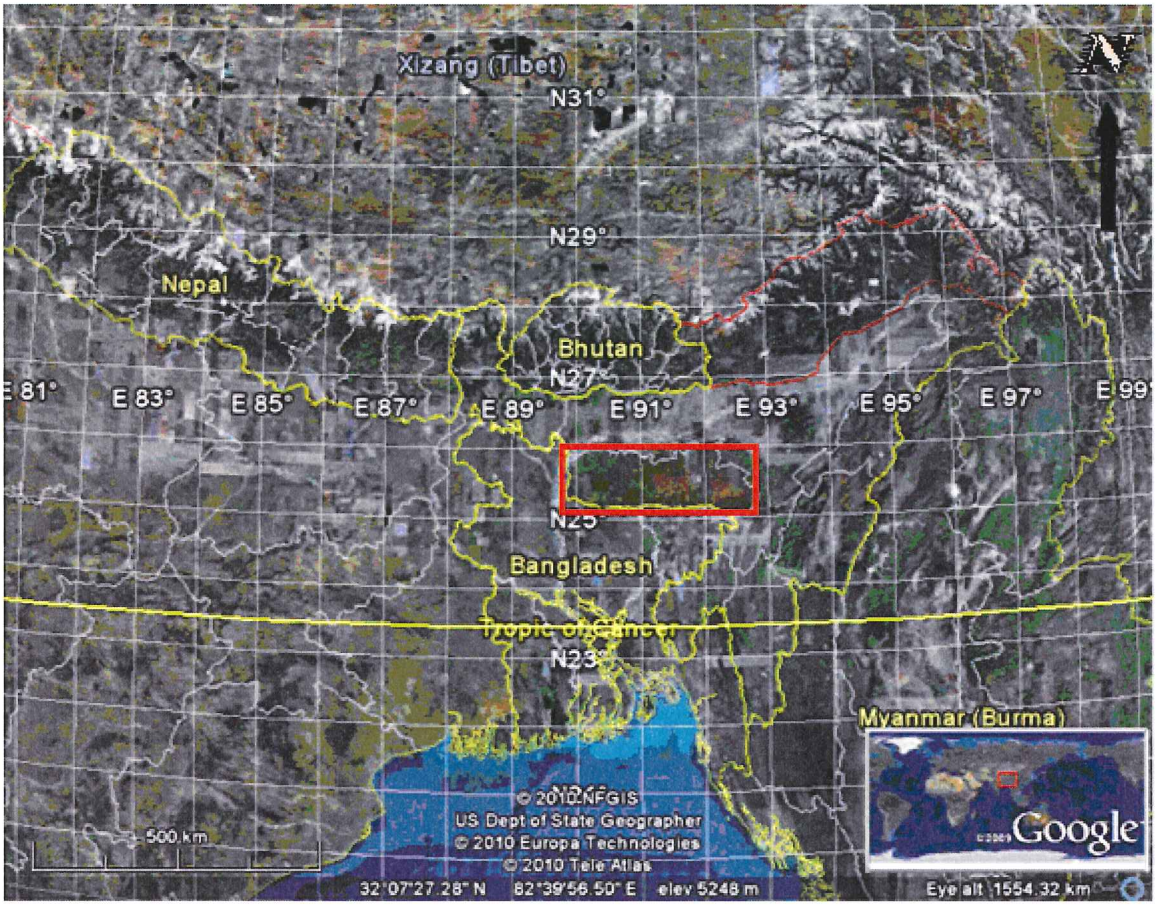

Figure 1.2: Google Earth image showing the location of Bhutan and neighbouring countries. The political borders are indicated by the yellow lines and the litigious international borders by the red lines. The thick-lined red box indicates the position of the Shillong Plateau (Google Earth).

1.2 Geological and structural characteristics of the orogen

The major structural and tectonostratigraphic features of the Himalayan orogen form an essentially continuous belt along the strike of the entire mountain range (Fig. 1.1). The major geologic units are separated by a series of north dipping thrust-fault zones originating from the collision of the Indian and Eurasian plates. The most southern structure, the Main Frontal Thrust (MFT) represents the toe of the Himalayan orogenic wedge and is typically depicted in cross sections as being the surface expression of a low

angle basal thrust, called the Main Himalayan Thrust, into which the Main Boundary Thrust (MBT) and Main Central Thrust (MCT) have their root (Fig. 1.1b). The Indian plate is subducting beneath Eurasia along the Main Himalayan Thrust (Hodges, 2000). The MBT which separates the Lesser Himalayan Sequence (LHS), a sequence of low-grade metasediments from more southern Tertiary Siwalik sediments preserved in the foreland basin while the MFT places the older part of the Siwalik section on top of more distal and recent (Late Tertiary to Quaternary) foreland basin deposits. The MBT dips shallowly (~35°) to the north, inferred from paleotectonic reconstructions of the frontal thrust system (Hodges, 2000). Further north, the MCT separates the LHS from the Greater Himalayan Sequence (GHS) (Fig. 1.1a), which are highly deformed meta-sedimentary and meta-igneous rocks including schists, gneisses and migmatites that were metamorphosed and deformed by the intrusion of Miocene leucogranites (Grujic et al, 2006). The MCT consists of a broad shear zone that dips moderately northward, sub-parallel to intense shear fabrics within the zone. In Bhutan, western India and Nepal, a series of half-klippens of GHS preserved south of the present-day trace of the MCT provide evidence for large displacements of tens to a few hundred kilometers along this structure. The most northern main structural feature is the Southern Tibetan Detachment (STD) which separates the GHS from the Tethyan Sedimentary Sequence (TSS) in southern Tibet (Fig. 1.1). In contrast to the previous thrust structures, the STD is characterized by normal sense of shearing interpreted as resulting from the extrusion of the GHS between the MCT and the STD. The hanging wall of the STD is made up of the TSS, a little deformed low-grade to unmetamorphosed marine sedimentary sequence.

1.3 Geology of Bhutan

The most southern geologic unit in Bhutan is the LHS (Fig 1.3). This sequence has historically been broken into several units; from the base to the top are: the Shumar Formation, the Daling Formation, the Baxa Group, the Diuri Formation and the Gondwana Sequence (Fig. 1.4) (McQuarrie et al., 2008). The Shumar formation is composed of recrystallized quartzite and has a varying thickness across Bhutan with a maximum thickness of 6 km; a key feature of the formation is the continuous planar bedding (McQuarrie et al., 2008). White mica and sericite define foliation within the Shumar Formation. The overlying Daling Formation is composed of up to 4-km-thick low grade metasediments. The lower contact is transitional from the Shumar quartzite moving into green phyllite at the base of the Daling changing to a chloritic to sericitic schist at the top. A 1.75 Ga age of a metarhyolite deposited within the Shumar-Daling Group helps constrain the age of the formations (McQuarrie et al., 2008). Above the Daling formation lies the Baxa Group which is formed of white to buff, gritty to pebbly quartzites, metasiltstones and greenish-grey to grey slates. McQuarrie et al., (2008) proposed that the minimum thickness of this group is approximately 2.5 km although it is interpreted to be tectonically repeated along 5 thrust faults. Above the Baxa lies the Diuri formation; a 2-2.5 km thick unit composed of diamicton interbedded with slates; the groundmass shows a clear schistosity within the unit (McQuarrie et al., 2008). At the top of the LHS lies the Gondwana sequence which is formed of feldspathic sandstone, siltstone, shale, coal lenses and plant fossils. Both the northern and southern boundaries of this sequence are faulted which makes it difficult to establish geometric relationships between it and the older strata of LHS. The total sequence thickness is ~2 km and its age

is Permian (McQuarrie et al., 2008). The LHS as a whole is interpreted as having been deposited on the northern Indian passive margin in the Proterozoic, a long time prior to the Eocene collision between India and Eurasia.

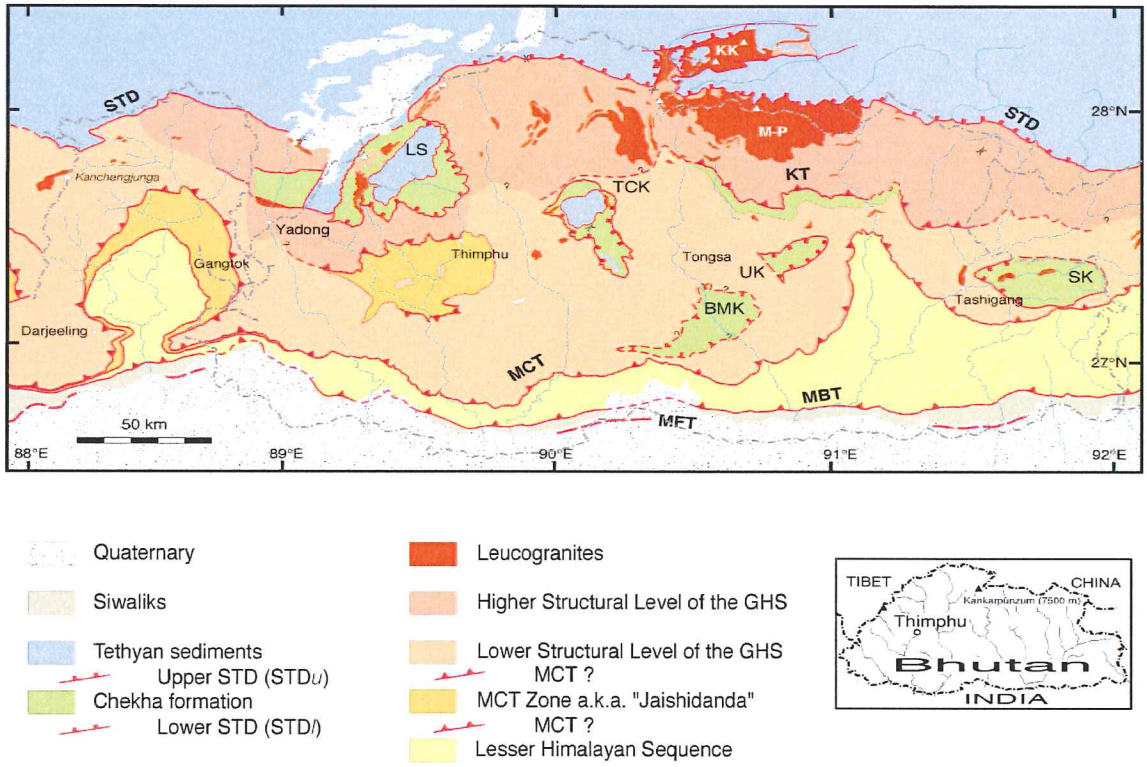

Figure 1.3: Map of the major structural and stratigraphic features along the orogenic front in Bhutan and Sikkim (Grujic et al., 2002)

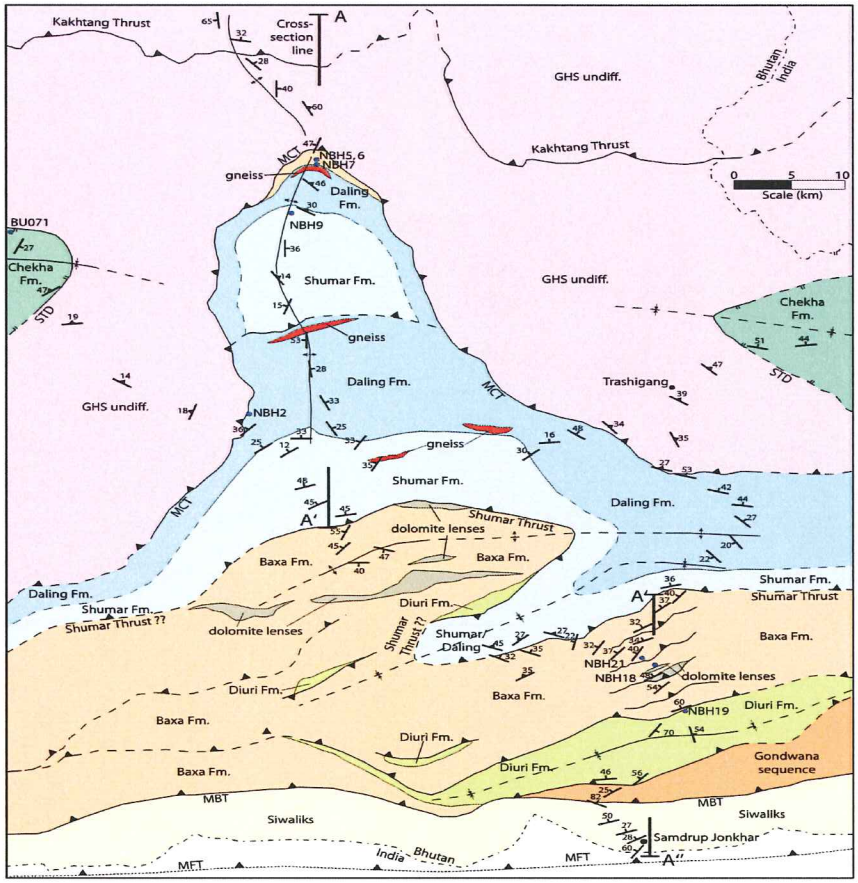

Figure 1.4: Geologic map showing the groups and formations of the LHS with an undifferentiated GHS lying above it. The MFT, MBT and MCT are also shown. The GHS is colored pink. The LHS units: the Daling Formation, the Shumar Formation, the Baxa Formation, the Diuri Formation and the Gondawana Sequence are colored dark blue, light blue, light orange, green and dark orange respectively. (Compiled by McQuarrie et al., 2008).

Structurally above the LHS lies the GHS which comprises the majority of the rocks exposed in Bhutan and is constrained between the MCT and STD (Fig. 1.3). Gansser (1983) subdivided the 60-100 km wide GHS into 3 parts; a gneissic unit, the Paro metasediments and leucogranite bodies. Granitic orthogneisses with centimeter scale k-feldspar porphyroclasts immediately overly the MCT; paragneisses, marbles, amphibolites and biotites schists are present but less common within this unit. Above this unit lie the Paro metasediments, which are dominated by metacarbonates interlayered with schists and quartzites along with amphibolites. Up section into the GHS, migmatites

become more common as well as leucogranite sills and dykes (Daniel, 2003). Discrete leucogranite bodies can be found throughout the entirety of the GHS and in some cases in the adjacent TSS. These bodies are the result of anatexis of the GHS crust and occur at a large range of sizes; they vary from centimeters to hundreds of kilometers. As a result of these granite bodies, partial melting of migmatites occurred. Then focused erosion, which removed the overburden, caused the ductile extrusion of GHS along its two bounding faults (Beaumont et al., 2001). Importantly, the GHS is bounded by a thrust shear zone at the base (MCT) and a detachment at the top (STD) and both structures have been shown to be active at the same time during the Miocene (Grujic et al., 2002). Having both and active thrust and normal fault bounding the GHS, with both senses of movement on the GHS side towards the surface, coupled with a ductile GHS, provides a dominant non-vertical exhumation pathway; this becomes important in chapter 3.

Structurally above the GHS in Bhutan is the TSS, which is bounded to the south by the STD (Fig. 1.3). These low-grade to unmetamorphosed marine sediments were deposited during the closing of the Tethys Ocean on the Eurasian margin (Hodges, 2000). Also overlying the crystalline GHS within klippen above the sequence is the Chekha Formation. This formation is bounded by faults interpreted to be part of a lower STD (Daniel et al., 2003). Metamorphic grade for both the TSS and Chekha formation decreases quickly as you move away from the STD; the dominant geology changes from garnet-staurolite schists at the base of the TSS and Chekha formation to low grade to unmetamorphosed sediments within a few hundred meters of the GHS contact (Daniel et al., 2003).

1.4 The Shillong Plateau

The Shillong Plateau, located within the Meghalaya state of northern India (Figs. 1.2 and 1.5) is an important component of the eastern Himalaya. Exhumation of the plateau, as documented by apatite fission track dating, began at least 9-15 Ma ago (Biswas et al., 2007) in the form of a pop-up structure bounded by two steeply dipping and seismically active thrust faults, the E-W trending north dipping Dauki fault in the south and the inferred WNW-ESE Oldham Fault in the north, it is also bounded to the east by the NW-SE trending Kopali fracture zone (Fig 1.5; Biswas et al., 2007); significant vertical displacement along the Dauki fault guided the exhumation of the Shillong Plateau. The basement of the plateau is primarily composed of Precambrian metamorphic and intrusive rocks such as granitoids, pegmatites and gneisses. Along the southern slope of the plateau flood basalts and alkaline-carbonatite complexes are found (early Cretaceous in age) (Biswas et al, 2007). On the southern fringe of the plateau there is up to 1000 m of Cretaceous-Tertiary sedimentary cover which are remnants of the original sedimentary cover before the exhumation of the plateau. The plateau itself is ~1600 m high on average and was uplifted due to the partitioning of horizontal convergence between India and Eurasia into both the Himalayan range front and Shillong plateau; however, this partitioning only accounts for ~10-15% of the total shortening experienced along the MFT (Biswas et al., 2007). This is a minor amount of partitioning and due to the displacement on the Dauki fault and subsequent uplift, the Shillong Plateau most likely did not have a significant impact on exhumation rates along the range front. Its surface uplift was decoupled from its exhumation, after the stripping of easily erodible sediments

from the harder basement below, at ~3–4 Ma at rates of 0.4–0.53 mm/yr which resulted in the creation of topography (Biswas et al., 2007).

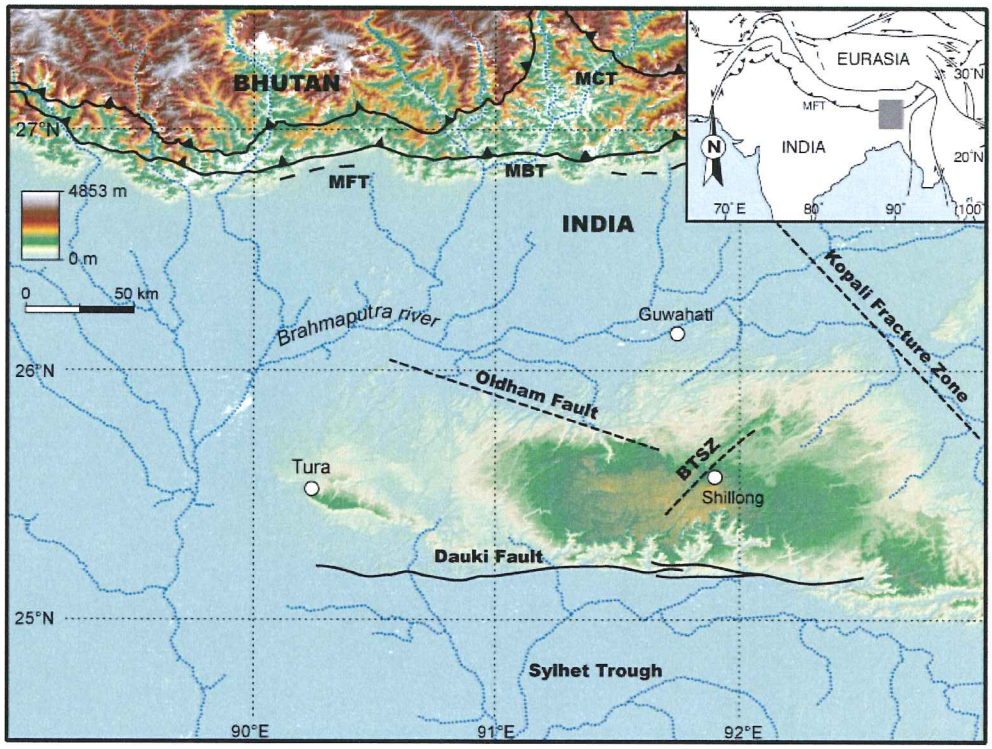

Figure 1.5: Digital topography and major structural features of southern Bhutan and of the Shillong plateau area (from Biswas et al., 2007 and references therein).

1.5 The Himalayan Monsoon

The main climatic feature driving erosion in the Himalayas is the Indian Summer Monsoon (ISM). The onset of the ISM is believed to have taken place by 20-35 Ma (Harris, 2006). The uplift of the Tibetan Plateau is thought to have had a profound effect on Cenozoic atmospheric circulation (Raymo and Ruddiman., 1992). As the southern flank of the Tibetan Plateau was uplifted, local heating occurred in the lower atmosphere and caused an area of low barometric pressure to develop; this caused warm and moist air from the Indian Ocean to be drawn towards the Tibetan plateau, where it was then forced upwards by the Himalayan range front. This warm air then condenses as it gets colder

and falls in the form of the intense focused precipitation that makes the region one of the wettest in the world. The monsoon travels from the Bay of Bengal toward the north in the eastern Himalaya, and then it is deviated westward along the strike of the range front (Fig. 1.6) (Bookhagen et al., 2005). Figure 1.7 shows the modern rainfall distribution along the Himalayan front.

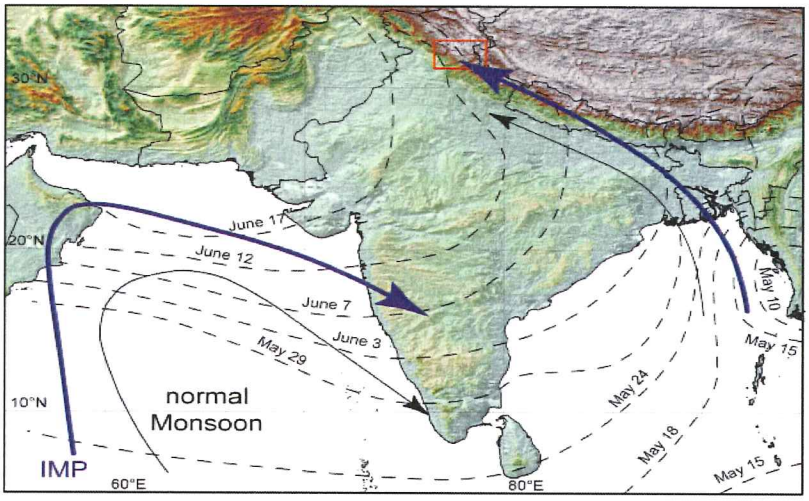

Figure 1.6: Map showing the path of the Indian Summer Monsoon between the months of May and June. Small black arrows show the current dominant wind direction for the monsoon. Bold blue arrows show directions of monsoon intensification in the Pleistocene and Holocene. Dashed lines show temporal evolution of the monsoon and its northwestward propagation through the season. These dates were inferred from satellite information and rain gauge measurements. (Bookhagen et al., 2005)

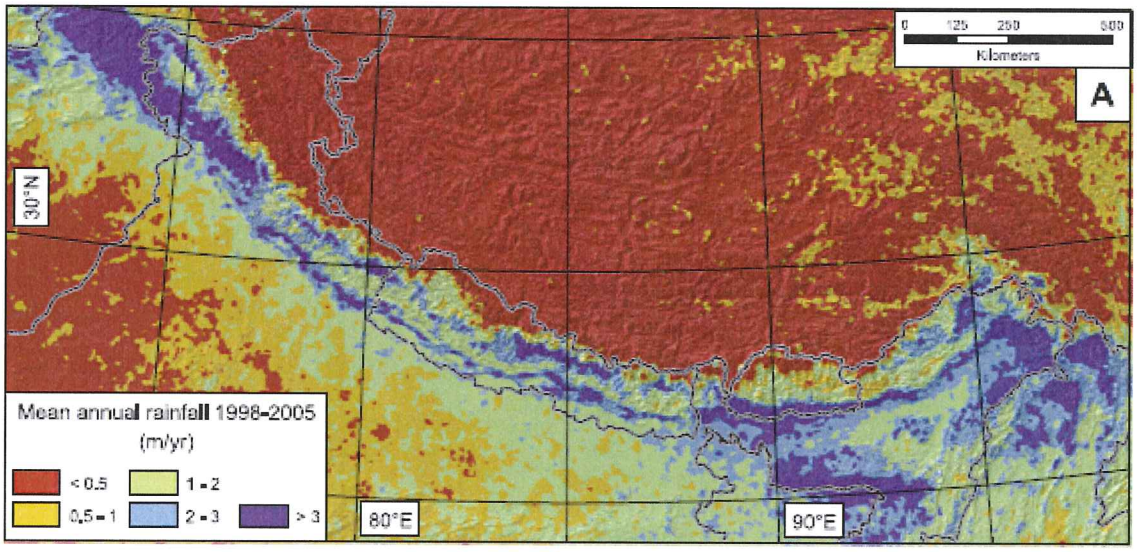

Figure 1.7: Raster image showing the mean annual rainfall along the Himalayan front between 1998 and 2005. The more intense precipitation occurs in a thin swath along the strike of the orogen due to the abrupt increase in elevation at this point. Bookhagen et al., 2006)

It has been hypothesized that the modern day Tibetan plateau is so high and broad that it affects climate not only on the scale of the monsoon but on a global hemispheric scale as well (Raymo et al., 1992). Ramstein et al., (1997) showed that Miocene shrinking and subsequent closing of the Paratethys Ocean also played a major role in the formation of the current ISM; as the Paratethys shrank, the amplitude of the seasonal cycles increased due to the proto-ocean no longer being a regional heat sink, leading to a dramatic increase in the frequency of the monsoon and therefore in the volume of precipitation delivered the Himalayas.

1.6 Rainfall Distribution across the eastern Himalaya

Precipitation distribution along the Himalayan Front is drastically different in Sikkim, Nepal and to a lesser extent, western Bhutan compared to the eastern Bhutanese Himalaya (Fig. 1.7). Figure 1.8 (from Grujic et al., (2006)) shows the different amount of precipitation along two profiles in eastern and western Bhutan, respectively. It shows while a large concentration of rainfall reaches the western Bhutanese front; the eastern Bhutanese front receives substantially less. A large concentration of precipitation is focused on the Shillong Plateau in eastern Bhutan while in western Bhutan the largest concentration of precipitation occurs at the base of the range-front. The discrepancy between the rainfall distributions in eastern and western Bhutan is attributed primarily to the presence of the Shillong Plateau (Grujic et al., 2006). Sedimentary and thermochronologic data suggest that the plateau began its uplift in the Pliocene (Biswas

et al., 2007). The 1600-meters-high E-W oriented plateau acts as an orographic barrier to the moist monsoon winds; up to 30-40% of monsoon rainfall is concentrated on the southern flank of the plateau and consequently a rain shadow is formed on its lee side. This rain shadow effect causes eastern Bhutan to receive about half of the precipitation as areas outside of the rain shadow such as western Bhutan, and further the Sikkim Himalaya in India (Fig. 1.7). Consequently, it is probable that until the uplift of the plateau, Bhutan had received a much larger volume of monsoonal rain than it does today (Grujic et al., 2006). Precipitation is much less at higher altitudes (above 1km) in Eastern Bhutan than in Western Bhutan (Fig. 1.8). Due to the concentration of large amounts of monsoonal rain on the Shillong Plateau, the majority of precipitation in Bhutan falls below 1 km. In Nepal, outside of the rain shadow, much more precipitation falls at higher altitudes than in Bhutan (Fig. 1.7).

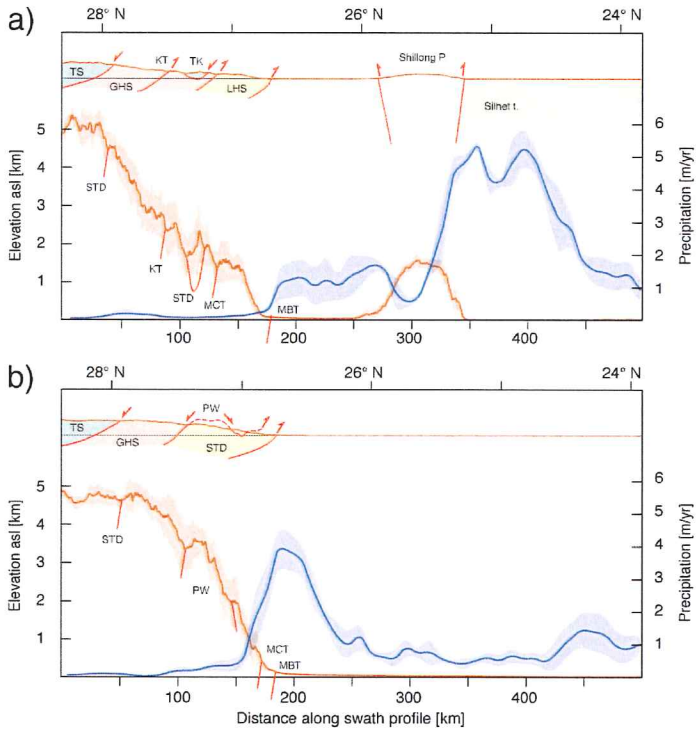

Figure 1.8: Two graphs showing the difference in precipitation patterns (blue), elevation (red) and geomorphology along two profiles, eastern Bhutan (Top) and western Bhutan (Bottom). (Grujic et al., 2006.)

1.7 Geomorphological Variations Along the Range Front

There are marked differences between the topography of the Eastern Himalayan front in Bhutan and further west along the range front. Figure 1.9 shows elevation, slope and geology in Bhutan and further west in Nepal (Duncan et al., 2003). Figure 1.10 shows the elevation profile of Nepal and Bhutan. Bhutan's topographic profile (Fig. 1.10b) is almost straight, with two slightly convex sections separated by a narrow, horizontal step at ~3000 m; this is due to the occurrence of an E-W trending belt of perched patches of low relief topography (Duncan et al., 2003). These patches are wide alluvium filled valleys composed of deeply weathered bedrock and do not follow lithologic or structural boundaries and are interpreted as relicts of an ancient landscape that was formed at lower elevation than its present-day situation (Grujic et al., 2006). The most likely cause for the preservation of this ancient landscape in the modern topography involves a sudden local climate change such as a decrease in precipitation inducing a significant reduction in erosion rate while rock uplift rate remained constant. This has led to the surface uplift of these smooth landscapes which had been originally formed at lower elevations (Grujic et al., 2006).

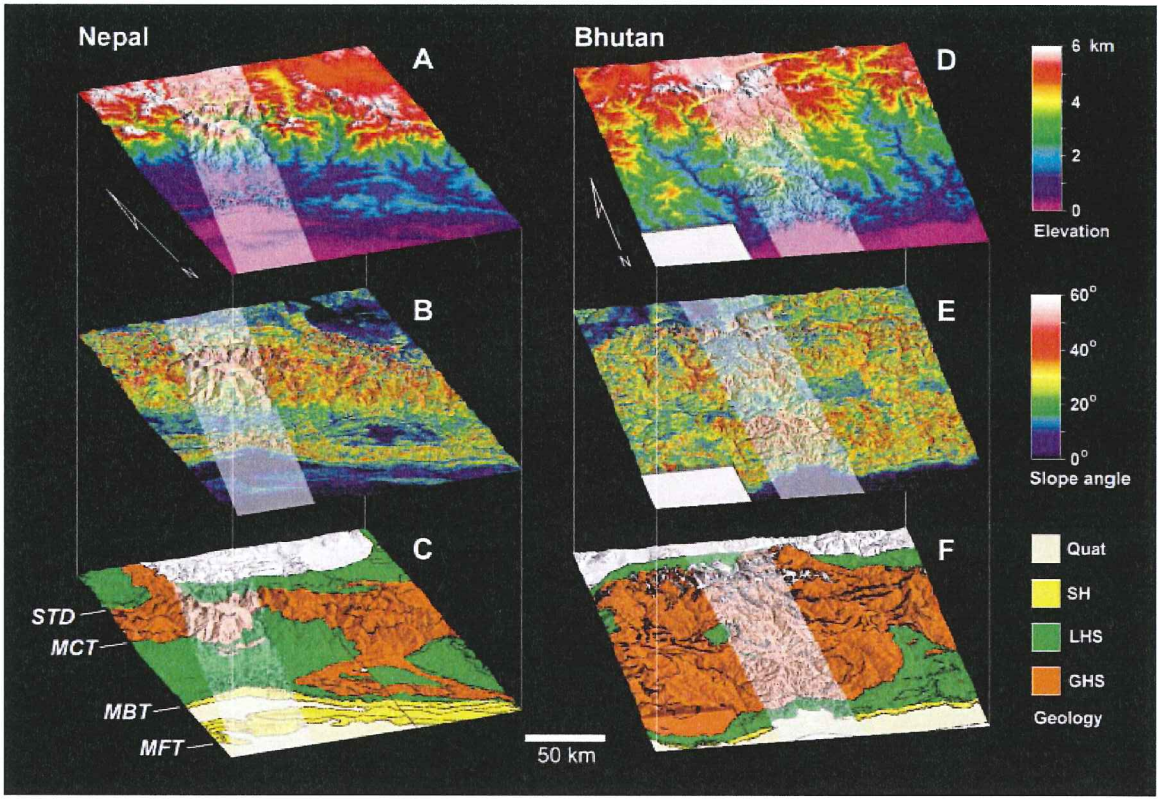

Figure 1.9- False color perspective views of elevation (A and D), slope (B and E) and lithology (C and F) comparing Nepal and Bhutan. (Duncan 2003)

From the base of the Himalaya, the Bhutan front rises less quickly than further west in Nepal (fig. 1.10). The rise to the highest peaks is much more gradual with ~90 km separating these peaks from the nearest elevations of ≤1000 m. Relief in Bhutan varies from 1000 m - 4000 m with the largest relief found in the more southern portion of the front (Duncan et al., 2003). Relief is important because it represents the difference between the highest and lowest points in an area which can show the depth of incision caused by flowing water and other erosive forces; areas with high relief may cause perturbations within the thermal structure of the sub-surface, but this will be explained in later chapters. In contrast, central Nepal (Fig. 1.10a) has a concave morphology and elevation rises quickly to the highest peaks; Nepal has a single step topology and slowly varying slope compared to the 3 steps topology of Bhutan. Hinterland relief is quite high

with just 20km separating the highest peaks from low valley elevations of <1000 m; steep slopes and channels along with deep fluvial dissection describe this zone (Duncan et al., 2003). The foreland of the Nepalese Himalaya comprises of a wide zone of lower relief.

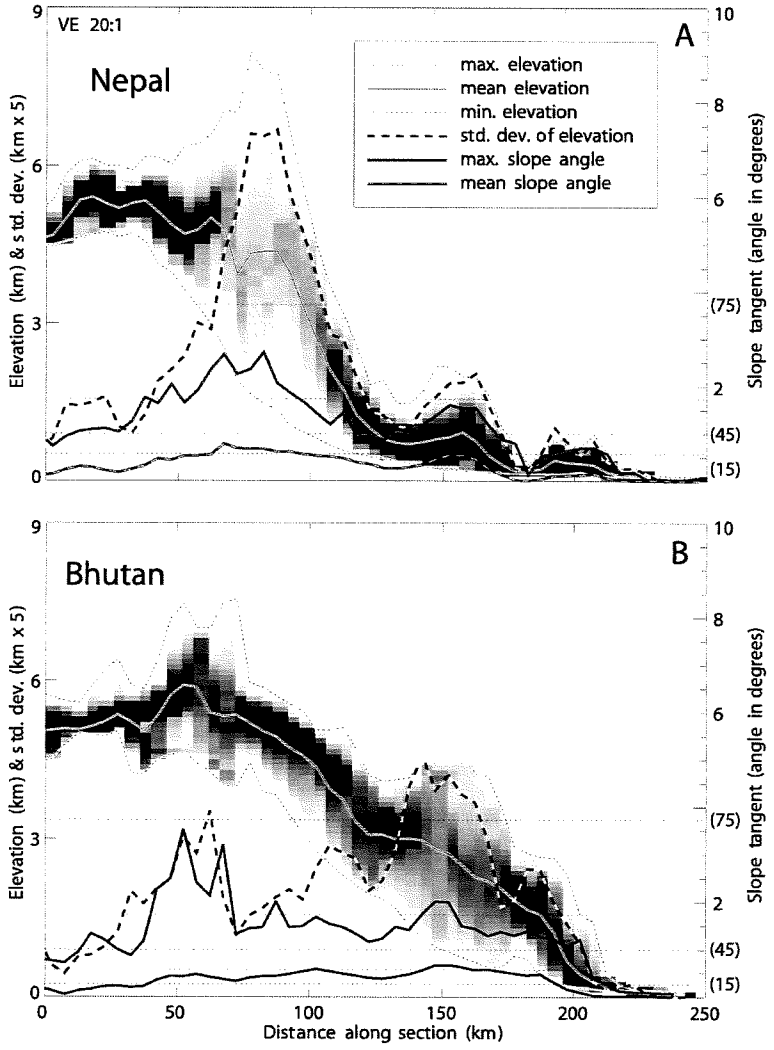

Figure 1.10: Profiles of elevation and slope for 50 km wide swaths in A) Nepal and B) Bhutan. Values sampled every 5 km along swath; maximum, minimum, and mean elevations and slopes are for each 5 x 50 km rectangle along swath. The different lines on the profiles, from the bottom of the graphs are as follows: minimum elevation, average elevation, relief and maximum elevation (From Duncan et al., 2003).

1.8 Anticipated Results

Apatite Helium (AHe) dating will be processed on four bedrock samples (see Table 1) collected along a vertical profile spanning ~18 km in length and 1990 m in elevation

from bottom to top in the Trumsing La area. This sample interval is within the GHS and was chosen due to it being located on the lee side, and within the rain-shadow, of the Shillong Plateau. As such, it receives less precipitation than areas outside the rain-shadow which makes it a useful locality in which to quantify changes in exhumation in the Pliocene (Fig. 1.11). AHe dating relies on the comparison of the relative concentrations of parent nuclides U, Th and Sm versus one of their daughter products, ^{4}He. ^{4}He atoms are created through alpha decay of U, Th and Sm, and are therefore given the name alpha particles. These particles are created at a known rate and thus any closed system (i.e. a mineral grain) that has both parents and daughter products can be dated using the AHe system. Previously published apatite fission track data on the same samples have yielded cooling ages between 7 Ma and 5.9 Ma and exhumation rates of 1.6±0.6 mm/year (Grujic et al., 2006). Apatite fission-track system is characterized by closure temperatures between 120-150°C and hence documents the exhumation of rocks from crustal depths between 5-6 km (assuming a constant geothermal gradient of 25°C/km). It is anticipated that our AHe ages will be younger (likely Pliocene) with exhumation rates that will either increase or decrease from the fission-track determined rates. There are several scenarios that may result from the data we obtain. A decrease in Pliocene exhumation rates with respect to Late Miocene could be attributed to the rain shadow effect triggered by the uplift of the Shillong Plateau in the Early Pliocene; a decrease in local precipitation rates would cause a decrease in local erosion leading to a decrease in exhumation rates.

Figure 1.11: A Google Earth image showing the locations of the samples BH104, BH103, BH101 and BH100/2 along the Trumsing La Pass. Sample BH103 is located very close to sample BH104 on this profile and as a result is hidden behind it at the scale necessary for this figure (Google Earth).

Deceleration of exhumation rates could also be attributed to a decrease in the rock uplift rate along the orogenic front. Indeed, partitioning of the convergence of the India-Eurasian collision into the Shillong Plateau has likely caused a decrease in the overall uplift rates in Bhutan to the North. This partitioning however only accounts for less than ~10-15% of the total convergence between India and Eurasia (Biswas et al., 2007). An increase in exhumation rates could have been caused by late Pliocene-Quaternary glaciations. The erosional effects from these glaciations are documented globally and surely have an effect on erosion of the Bhutan Himalaya. Another possible cause for

increased local exhumation rates could be renewed tectonic activity along the range front though this has yet to be documented.

Chapter 2: Methodogy

In this Chapter, the AHe isotopic system, analytical procedure for both He extraction and parent isotope extraction and age calculation equation will be explained in detail.

2.1 Apatite Helium (AHe) Dating Isotopic System

This dating method relies on the ingrowth of α-particles produced by U, Th and Sm series decay; α-particles being completely ionized helium atoms or ^{4}He. ^{147}Sm initially present (that is not created from U or Th decay within the crystal) also degenerates by α-decay contributing to the overall ^{4}He concentration; in most cases however the contribution is insignificant (≤1%) because Sm only goes through 1 α- decay during its decay chain. Sm is also usually present in smaller concentrations than U and Th. (Farley and Stockli, 2000). As a result of the radioactive decay, the α-particles are ejected a measureable distance from the site of the decay before coming to a rest within the crystal lattice. At temperatures higher than the closing temperature of the crystal (~70°C for apatites of size 80-90μm in radius), ^{4}He is not retained in the grains due to thermal diffusivity (Farley and Stockli, 2000). At temperatures lower than the closing temperature, ^{4}He is partially retained in the grains and since radioactive isotopes decay at a predictable rate, AHe ages are calculated by measuring the concentration of the parent isotope (^{238}U, ^{235}U, ^{232}Th and ^{147}Sm) and the daughter isotope (^{4}He) in apatite grains. As a result of having such a low closing temperature, the ages acquired from AHe dating are not crystallization ages but rather the age at which a particular grain moved through a point at depth equivalent to its closing temperature. This is simply called a cooling age.

The equation for helium ingrowth is as follows:

$$^4He = 8\left(\frac{137.88}{138.88}\right)^{238}U(e^{\lambda_{238}t}-1)+7\left(\frac{^{238}U}{138.88}\right)(e^{\lambda_{235}t}-1)+6^{232}Th(e^{\lambda_{232}t}-1)+1^{147}Sm(e^{\lambda_{147}t}-1)$$

(2.1)

This equation shows the number of α-particles produced by each of the parent isotopes before they become inert. ^{238}U, ^{235}U and ^{232}Th go through 8, 7 and 6 α-decays respectively by the time the reaction series (Fig. 2.1) ends with lead isotopes (^{206}Pb, ^{207}Pb and ^{208}Pb respectively). The extra factors of 137.88/138.8 and 1/138.8 attributed to ^{238}U and ^{235}U reflect the natural abundance of ^{238}U compared ^{235}U ($^{235}U/^{238}U$=1/138.8) (Table 1). ^{147}Sm is represented in the equation by a single α-decay due to its extremely long half life ($(1.05\pm0.02)\times10^{11}$) and short decay chain (Only a single α-decay from parent ^{147}Sm to final daughter ^{143}Nd). As a result, ^{147}Sm in apatite can be ignored in most cases except when ^{147}Sm concentrations are high. A notable exception is the Durango apatite, which we use as a standard in our dating because it has relatively high concentrations of ^{147}Sm. ^{147}Sm will not be ignored in our calculations because our samples have high enough concentrations of the isotope to have some effect on the final age. One of the assumptions made when using the above equation is that no atmospheric He is present naturally in the sample. This is most likely a valid assumption because the amount of He present in the Earth's atmosphere (~5ppm) is insignificant (Farley, 2000). It is also possible for He to be trapped in fluid inclusions due to some earlier magmatic event; this will be addressed in the error section below.

a)

Isotope	*Abundance* (%)	*Half-Life* (yr)	*Decay Constant* (yr^{-1})	*Thermal-Neutron Capture Cross-Section* (σ) (10^{-24} cm^2)
^{232}Th	100.0000	1.41×10^{10} (α)	4.916×10^{-11} (α)	7.4
^{234}U	0.0057	2.47×10^{5} (α)	2.806×10^{-6} (α)	100
^{235}U	0.7200	0.7038×10^{9} (α)	9.8485×10^{-10} (α)	580
^{238}U	99.2743	4.468×10^{9} (α) $\sim 1.3 \times 10^{16}$ (s.f.)	1.55125×10^{-10} (α) $\sim 7.5 \times 10^{-17}$ (s.f.)	2.7

b)

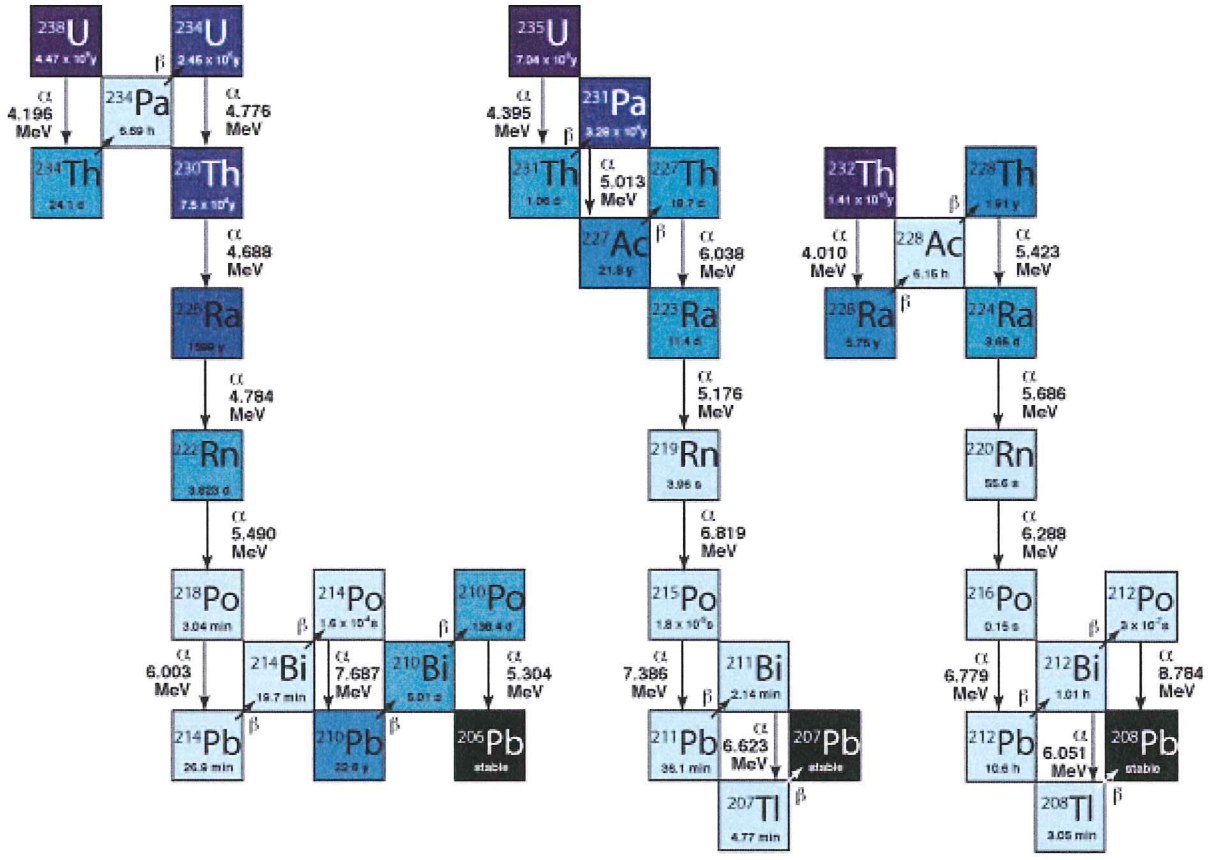

Figure 2.1a: Abundance, half-life, decay constants and thermal-neutron capture cross-sections for U and Th isotopes. Compilation from ERTH 6400 slide show by Konstanze Stubner. Figure 2.1b: The decay series of 238U, 235U and 232Th. Vertical translations represent α-decays and diagonal translations represent beta-decays (MacQuarie University website).

2.2 Sources of Error in Ages

There are several situations in which crystals will give unreliable ages. The most common sources of error have to do with crystal purity, size and shape. Mineral and fluid inclusions are the greatest sources of error when dating apatite (Farley, 2002). Mineral inclusions can skew ages obtained from apatite grains and make them date older than they actually are. This happens because α-particles will eject from the inclusion into the lattice of the apatite and get measured while the parent isotopes may not, depending on the properties of the inclusion. Common mineral inclusions within apatite include zircon, monazite and xenotime (Farley, 2002). These three minerals also contain radioactive elements like U, Th and Sm that produce α-particles similarly to apatite. The problem lies in the fact that some of these minerals don't dissolve as readily as apatite and they have different closing temperatures (or are characterized by different diffusivity for ^{4}He). Zircons in particular are a problem because they produce a lot of α-particles but require a stronger acid than is used in the AHe technique to dissolve them and measure U, Th and Sm concentrations. Zircons also have a higher closing temperature than apatite (~180°C) which means they would begin to emit α-particles sooner, in an exhumation induced cooling scenario, and take longer and higher temperatures to completely de-gas than apatite. This could lead to errors both in the parent isotope and daughter product concentrations. Fluid inclusions can also be detrimental to the ages obtained if the fluids have a concentration of α-particle producing nuclides that is measurably different than that of the host crystal. Fluid inclusions like this will also give older than normal ages however problematic fluid inclusions are rarer than mineral inclusions (Farley, 2000).

The size and shape of crystals are also crucial for dating accuracy due to α-particle ejection.

2.3 α-particle Ejection and Correction

As α-particles are created from the breakdown of isotopes, they are ejected ~20 μm away from the site of the reaction due to the immense amount of kinetic energy released (Fig. 2.2) (Farley, 2002). As these reactions occur within the outer 20μm rim of a crystal, a certain proportion of α-particles are ejected out of the grain and as a result are lost. To account for this fact, an α-correction (Ft) is applied to the crystal; this is a mathematical equation to correct for the loss of α-particles that depends on the size and geometry of the grain in question. The result is a factor by which the age of the grain must be divided (corrected age=Measured age/F_T), (Fig. 2.3). If there is a larger volume of crystal compared to the constant 20μm depleted outer rim then the error caused by this α-particle ejection will be minimized so the larger the grain is, the better the correction will work.

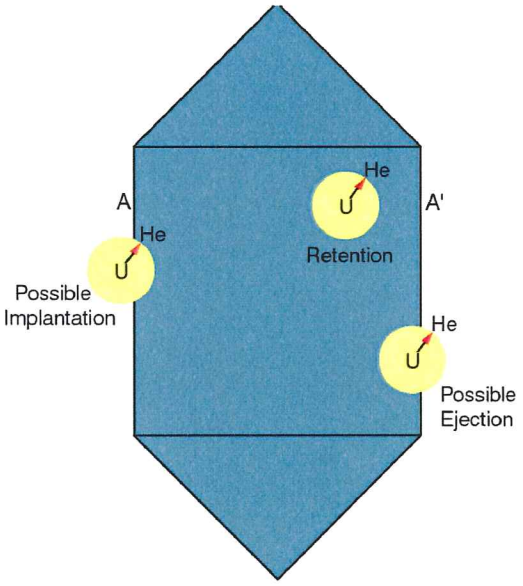

Figure 2.2: A diagram showing the possible paths of an α-particle within a hexagonal prism shaped crystal. Farley, 2000

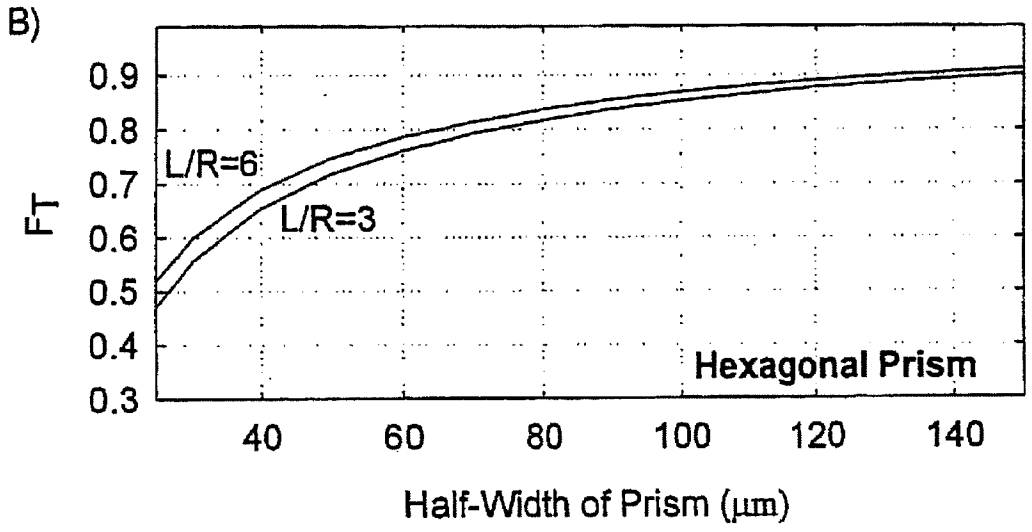

Figure 2.3: A graph showing the relationship between Ft and the half-width of a hexagonal prism. Note that even as the ratio of length to radius of a crystal doubles, Ft does not drastically change. This shows that the radius of a prismatic grain has more control on Ft than its length. Farley, 2002.

The correction is calculated for a perfectly euhedral grain with the shape of a hexagonal prism. The closer to this ideal geometry our grains will be, the lower the error will be when applying the correction. Furthermore, α-particle injection can also happen (Farley, 2002). This occurs when α-particles eject from nearby grains in the host rock and are injected into the lattice of the crystal in question. The two grains need to be less than 20 μm apart for this phenomenon to happen and consequently, α-particle injection, is much rarer than ejection and may be neglected (Farley, 2002).

Zonation in apatite grains is an important factor to take into account when applying the α-correction. Since the correction assumes a homogeneous distribution of parent isotopes, severely zoned grains would yield erroneous ages. This is especially true for reversely zoned crystals where a greater proportion of parent isotopes reside in the outer rim. Such heterogeneous distribution increases the probability of α-particle ejections happening and

thus obtained ages would be younger than for an isotopically homogeneous grain corrected similarly. Conversely, a "normally" zoned crystal with higher parent isotope concentrations in the core would produce an older age if a normal α-correction was applied. Error produced by zonation is compounded further by helium lost due to diffusion.

2.4 Helium Loss by Diffusion

Knowledge of how helium diffusion rates change through different temperatures is paramount to AHe thermochronometry because it controls the closing temperature of apatite. This knowledge is impossible to obtain from a natural setting due to the large time scale involved in He diffusion; it is instead taken from laboratory experiments. Because of time constraints, laboratory experiments are performed on a shorter time scale (minutes to days) and at higher temperatures which increase the rate of diffusion to measureable values (Ehlers and Farley, 2003). Samples of the mineral in question are heated progressively and the emitted He measured at each step providing a detailed analysis of diffusion behavior as temperature changes. These laboratory measurements must then be extrapolated for use at lower temperatures. This extrapolation can see diffusivity change by up to 4 orders of magnitude; this may cause relatively small errors to become much larger when applied to relevant temperatures (Ehlers and Farley, 2003). Diffusivity studies done on the standard and well-calibrated Durango apatite have shown that for temperatures below ~300°C, the diffusivity of apatite obeys an Arrhenius relationship (Farley and Stockli, 2000).

Several studies have attempted to correlate the relationship between age and elevation obtained in the laboratory to values measured from natural settings. For example,

experiments done on boreholes with a known thermal gradient usually show a rapid decrease in He ages as a function of depth (Farley and Stockli, 2000). At relatively great depths (greater than ~3km) , ages of apatite grains will essentially equal zero because helium is fully lost due to high temperatures (greater than ~80°C). At lower temperatures (<40°C), all helium is accumulated and retained within the grain and ages represent the time at which the section was cooled. The zone between the depth of no retention and full retention is known as the Helium Partial Retention Zone (HePRZ) (Reiners and Brandon, 2006). The bounds of this zone are represented by the temperature at which 10% of helium is retained (the deep boundary) and the temperature at which 90% of helium is retained (the shallow boundary) (Fig. 2.4). The depth of the HePRZ depends on the geothermal gradient at depth in the sample area.

Zonation of apatite crystals affects He diffusion in the same way it affects He ejection; the higher the concentration of parent isotopes in the outer rim of the grain, the shorter the distance an He atom needs to travel before it can diffuse out of the grain which results in a younger than expected age. Diffusion however is primarily affected by temperature. Diffusion occurs more rapidly at higher temperatures which suggests that a fast cooling crystal will be younger than a relatively slow cooling crystal. This is because the fast cooling crystal retained more of its He due to spending less time within higher temperature zones. (Ehlers and Farley, 2003).

2.5 Effective Closure Temperature

Due to the existence of the HePRZ, closure of apatite crystals does not occur at a specific temperature, but over a range of temperatures (Reiners and Brandon, 2006). Despite this closure temperature range, the AHe method (as well as other thermochronometers) will

yield a cooling age, which corresponds to the time at which the grain cooled below a single temperature, the effective closure temperature (T_c), assuming a steady monotonic cooling history (Reiners and Brandon, 2006); Tc is a function of the activation energy, frequency factor, cooling rate and geometry and size of the grain (see Reiners and Brandon, 2006). In nature, the assumption that AHe data will point to a single date is often valid, given the narrow temperature range of the HePRZ compared to the PRZ of other thermochronometers (such as He titanite and He zircon (Fig. 2.4) and the fast response of the closure isotherm of the AHe system to external changes (Fig. 2.5).

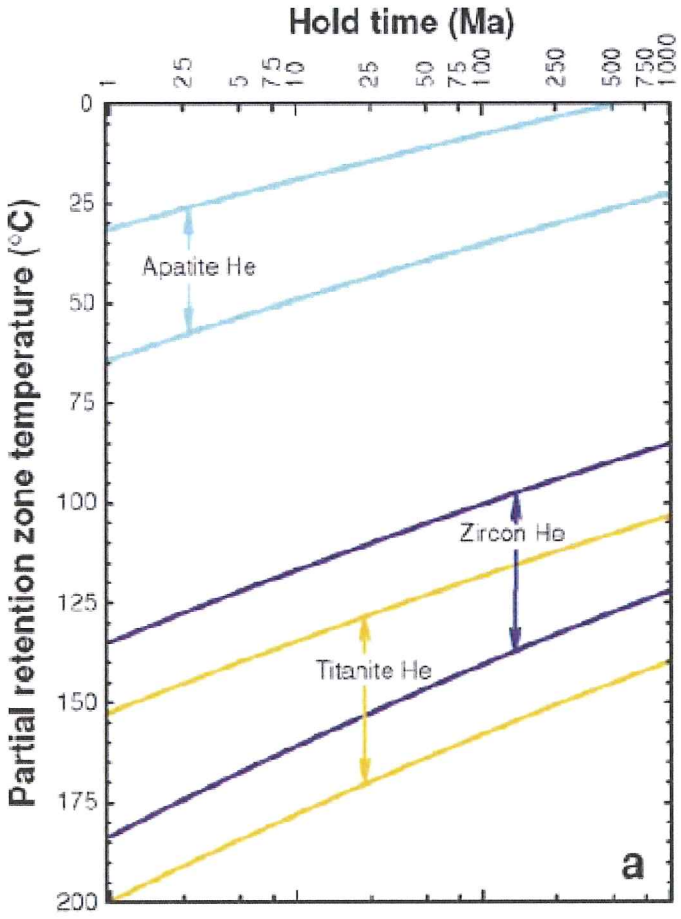

Figure 2.4: Diagram showing the temperature range of the apatite, zircon and titanite HePRZ over time. The upper and lower bounds of the PRZ for each thermochronometer represent the 90% and 10% He retention point respectively, after being held at a steady temperature for a specific amount of time (Reiners and Brandon, 2006).

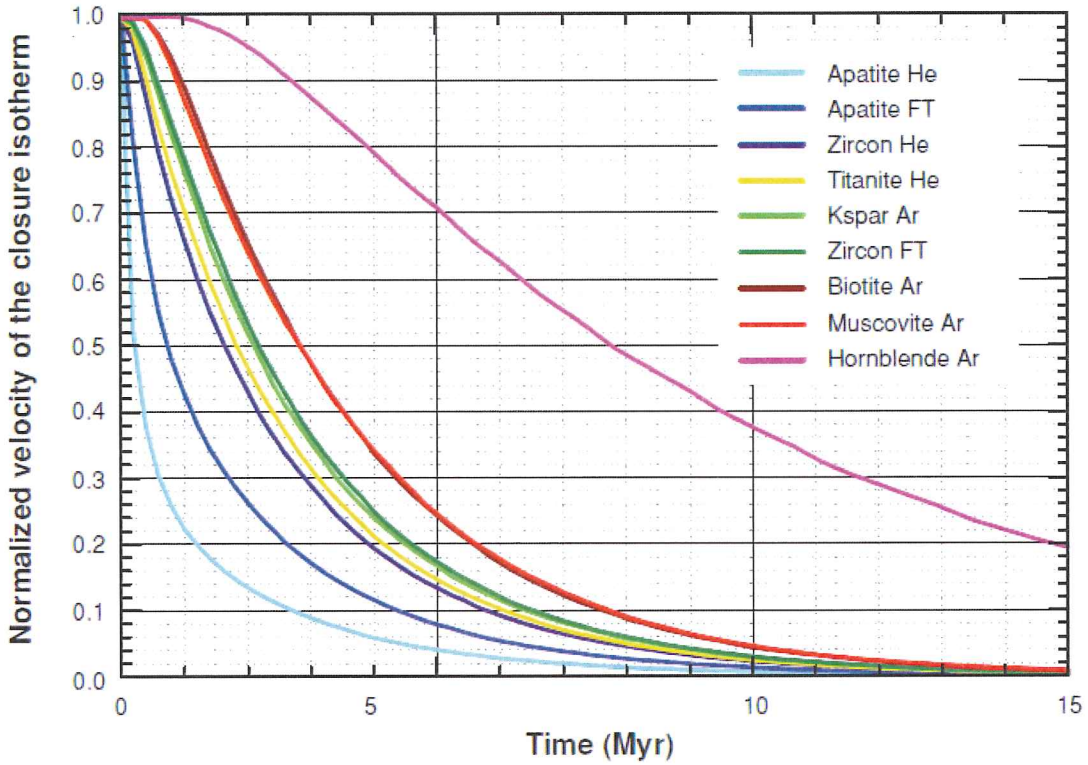

Figure 2.5: Response of the closure isotherm to the sudden onset of rapid erosion from 0 to 1 km/Ma. The curves show the normalized velocity of closure isotherms with time after the initiation of rapid erosion for the common He, FT, and Ar thermochronometers. The normalized velocity is defined as the vertical velocity of the closure isotherm divided by the erosion rate. A normalized velocity of one means that the closure isotherm is moving with the same velocity as the rock relative to the surface. A normalized velocity of zero means that the closure isotherm has recovered fully to its steady state depth. Note that the apatite He system has the fastest response time (From Reiners and Brandon, 2006).

2.6 Preparation of the Samples

The initial collection of the samples and separation of the apatite crystals were performed by Isabelle Coutand. The apatite crystals were then immersed in ethanol and placed under a stereoscopic microscope at a 106.6x magnification under transmitted light for visual inspection and selection of the grains to be used for AHe analysis. The grain picking was done primarily on the basis of grain shape; since grain shape is the main parameter that decides the α-correction. The majority of the grains were cracked or highly anhedral; the

grains chosen for final selection ranged from euhedral hexagonal prisms with both ends intact to subhedral egg shaped grains with blunt ends. After finding a grain with an acceptable shape (Fig. 2.6), it was examined under cross-polarized light in order to find small mineral and/or fluid inclusions. The size of the crystal is also of critical importance due to the application of the α-correction factor F_T. The bigger the crystals, the smaller the correction that needs to be applied; in particular, the smallest β possible, defined as the surface area to volume ratio of the grain, is ideal.

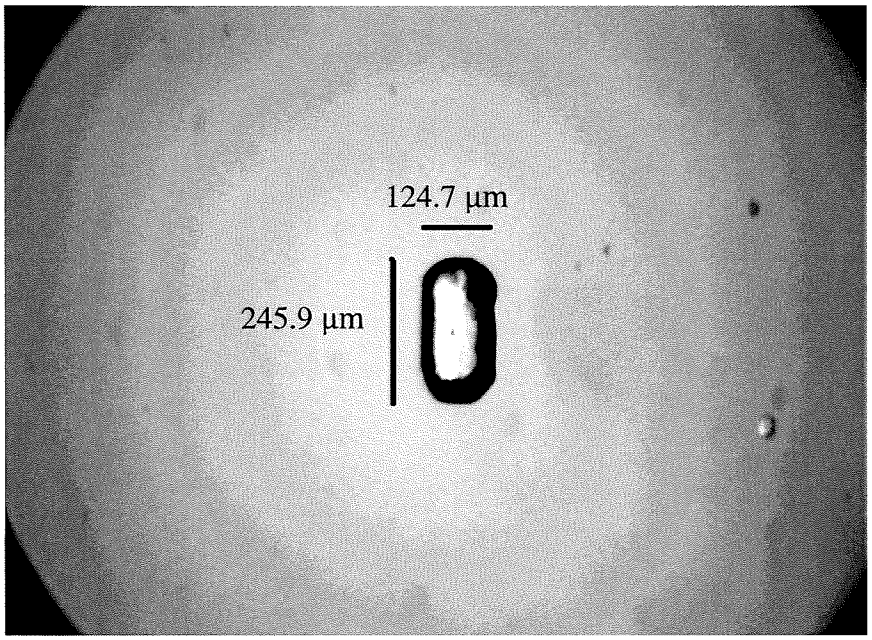

Figure 2.6: Pax-it photograph of sample BH100/2-grain #4. This grain was reasonably well shaped with two axes being similar and the third being longer. A small fluid inclusion is visible in the center of the crystal. Full descriptions of the grains can be found in appendix A.

Grains with mineral inclusions of any kind were generally discarded although grains with small fluid inclusions were chosen when no other alternative was present. Ten grains were preselected for each sample to go to final selection on the basis of shape, size and freedom from inclusions. This final selection involved thoroughly checking each grain for inclusions; the grains were flipped around on several faces so that when under cross-polarized light, inclusions would show strong interference colors when the surrounding grains went extinct. A total of 4 grains were finally selected for each of the 4 samples and

these grains were photographed and accurately measured using Pax-It, a computer program that integrates a camera onto the microscope. After the software was calibrated using a micrometer, 3 different axes (x, y, and z) were measured on each grain for later use in the application of the α-correction. Each grain then needed to be placed inside a platinum crucible for analyses and transport. These crucibles were first immersed in a 5% solution of nitric acid for >12 hours to etch them in order to remove any potential uranium contamination. To seal the grains within the platinum tubes, one end of the tube was first pressed flat with a pair of tweezers. The grain was then inserted into the tube and the other end of the tube pressed flat with the grain inside. In addition to this, apatite grains of known age and composition (Durango apatites) have been packed to serve as standards. Three empty etched platinum foils were also analyzed for use as blanks. The measurements performed on these standards and blanks will help calibrate and assess the quality of our results on "real" samples.

2.7 He Extraction

The samples were degassed of their helium in the Dalhousie University Argon Geochronology laboratory. The samples were heated to 1050°C for 5 minutes to de-gas the bulk of He from an apatite crystal without melting it. A laser was used to heat the samples and since the grains were packed within the platinum crucibles, they were not subjected to direct heat and are less likely to volatilize and lose U or Th (Farley, 2002). The helium extracted from the crystal is then vacuumed into a chamber and measured with a quadrupole mass spectrometer, which measures the concentration of all helium isotopes within the sample. To increase the resolution of the quadrupole mass spectrometer, isotope dilution is used. ^{3}He and ^{4}He are measured in 2 solutions: one with

a standard solution and a spike, and the other with the unknown sample and a spike. A spike is simply a small amount of sample enriched, in this case, with ^{3}He. Measurements of He will actually measure the ratio of $^{3}He/^{4}He$ in the unknown sample; using this ratio, and the concentration of the isotope spike added, the concentration of ^{4}He within the samples can be calculated. A re-extraction is processed to ensure that all the Helium contained in the grain was collected. If a substantial amount of He is detected during the subsequent extraction, it is classically attributed to the presence of parent-isotopes-rich solid inclusions in the apatite grain, such as the common zircon inclusions observed in apatite crystals. In particular, zircon has higher closure temperatures than apatite and will not be completely de-gassed at the temperatures and within the time periods used in the procedure adequate for apatite. If the percentage of re-extraction exceeds 0.15% the grain is generally discarded.

2.8 U, Th and Sm Extraction

The samples were sent to our collaborator, MG. Fellin (Zürich polytechnic school, ETH Zürich) for destructive U, Th and Sm concentration measurements. First, the platinum crucibles with the apatites inside are placed inside Teflon vials. Then 1ml of spike containing ^{233}U and ^{229}Th are added. HNO_3 is added next until the final concentration of the acid is 5%. Finally, 2 drops of HF is added. The vials containing this solution are sealed tightly and put on a hotplate at 120°C for 24 hours and then dried to near zero moisture content. After the drying, 1ml of 1% concentrated HNO_3 is added; the solution is then left to homogenize on the hotplate again at 60°C for 1 hour. After the hour, the sample is cooled for up to 24 hours. The sample is then ready to be put through the ICP-MS. HNO_3 is used because it is strong enough to dissolve apatite but will leave the

platinum tube intact. This is important because Pt can interfere with measurements of U; Pt can combine with the Ar used to nebulizer. These Pt/Ar molecules have an atomic weight of 234 amu which is close enough to the weight of ^{235}U to cause problems. Concentrations of U, Th and in this case Sm are then measured directly from the solution using an inductively coupled plasma mass spectrometer (ICP-MS). The solution is nebulized into an aerosol and sprayed through a jet of plasma created by superheating argon gas. This plasma removes all traces of solvent and ionizes the sample. A quadrupole mass spectrometer is used to create an ion beam which is bent by powerful magnets depending on the weight of the isotope. The degree of bending of the beam is what separates the different isotopes of U, Th and Sm. These concentrations can then be measured. Once both the amount of parent isotopes and daughter products are known, then an age can be calculated.

2.9 Determination of Ages from Parent/Daughter Ratios

Ages cannot directly be measured from U, Th, Sm/He ratios; they must be indirectly calculated through a Taylor series and then reiterated integration. A Taylor series is an approximation of a function as a sum of terms calculated from the values of its derivatives at a single point and is written as:

$$\sum_{n=0}^{\infty} \frac{f^{(n)}(a)}{n!}(x-a)^n \qquad (2.2)$$

$f^{(n)}$ = n derivative

a = single point/starting point (x_0)

(x-a) = delta between the starting point, a, and any x value of the function

$f^{(0)}(a) = f(a)$

In the case of AHe dating, the function input into the Taylor series is the He ingrowth equation shown earlier (Equation 2.1). Once the Taylor series has been solved, a guess must be made for the actual age of the apatite grain. This guess functions as t_0 in the final Taylor expression, which is solved for by substituting Equation 1 into Equation 2 and further integrating:

$$
\begin{aligned}
{}^4He &\approx f(t_0) + (t_1 - t_0) f'(t_0) \\
{}^4He &\approx f(t_0) + t_1 f'(t_0) - t_0 f'(t_0) \\
t_1 f'(t_0) &\approx {}^4He - f(t_0) + t_0 f'(t_0) \\
t_1 &\approx \frac{{}^4He - f(t_0) + t_0 f'(t_0)}{f'(t_0)} \qquad (2.3)
\end{aligned}
$$

Using t_0, t_1 can be approximated by solving the above equation. The relative error between t_0 and t_1 is then calculated using the following equation:

$$\in_a = \frac{t_1 - t_0}{t_1} 100 \qquad (2.4)$$

If Ea is >5%, then a t_2 must be calculated because the error is too high. t_2 is calculated using equation 3 in the same way t_1 was calculated except t_1 and t_2 are substituted for t_0 and t_1 respectively. This can be continued to t_n, further reducing the error until it is acceptably small enough (<5%). The final t_n calculated is then the raw age given to the sample. To get the final age of each grain, the raw ages obtained must be divided by the α-ejection factor (Ft). This factor takes into account the daughter products lost through ejection from the crystal.

Chapter 3: Data and Interpretations

In this chapter, the data acquired from He extraction and ICP-MS analysis of U, Th and Sm concentrations will be presented and interpreted. A description of some of the limitations encountered in this study will also be outlined. Finally, with both the parent isotope and daughter product concentrations determined, the ages of our grains can be calculated through an iterative process outlined in the previous chapter. These ages are presented and interpreted at the end of this chapter along with a comparison between the obtained AHe ages and previously calculated AFT ages.

3.1 Helium Concentration Results

The He concentration results obtained from the noble gas lab at Dalhousie University are presented in Table 1. The amount of He extracted, measured in femtomoles (fmols), ranges between 1.38-9.28 fmols, with more than half of the samples falling between 1 and 3 fmols (Table 1). The one glaring exception is Sample BH100/2 that yielded very low amount of ^{4}He with values of -0.02 - 0.07 fmols (Table 1). These concentrations are outside the detectable limits of the instruments, as shown by negative values. The comparatively very low values of He for all 4 grains of sample BH100/2 may be due to three causes 1) the grains from this sample were initially depleted in parent U, Th and Sm, 2) the presence of tiny fractures or other physical damages may have lead to an increased rate of diffusion and consequent He loss from the grain or 3) the grains cooled very recently through the PRZ and ^{4}He did not have enough time to accumulate. Most likely the low He values are a result of low parent U, Th and Sm as seen from grain BH100/2-1 on table 2 (only this grain was analyzed to confirm that the parent isotope values in the sample were below the ICP-MS detection limit). This sample will not be

included because the small fraction of He measured precludes the calculation of any relevant age. Another set of useful values presented on Table 1 are the re-extraction measurements (in fmols and % of original He extraction). A positive re-extraction means that after a second round of heating the grain, a significant amount of ^{4}He (in our case >0.15fmols or >0.75%) has been extracted and measured. This is a potential issue because a significant positive re-extraction can indicate the presence of unseen and undocumented α-particle producing mineral and/or fluid inclusions which could lead to an artificial increase in the concentration of He in the samples. This occurs because the mineral inclusions contribute α-particles but may not release gasses as readily as the host apatite. Also, the concentration of parent isotopes within inclusions may not be the same as in the host apatite and therefore could increase or decrease the overall concentration of He in the grain. In the case of stronger minerals such as zircon, which require higher temperatures than apatite to fully extract He, complete extraction of He will not occur leaving measureable amounts of He within the inclusion; this latent He will be measured on subsequent re-extraction analysis. This can be a useful result however because it gives us information about the possibility of implantation of α-particles from these inclusions into the lattice of our grains. However, because He will be produced from these inclusions in different proportions than from the host mineral of interest, the final He concentration will be artificially skewed. Re-ext % is more useful than just the re-extraction concentration because the % shows the proportion of He extracted compared to the concentration of the original He extraction. At least 3 of our remaining 12 grains have a positive re-extraction (BH104-4, BH103-1, and BH101-4 have Re-ext % of 8.07%, 7.21% and 2.81% respectively, (table 1) which are most likely the result of unseen

mineral inclusions. Grain BH101-1 is not positive using Re-ext % but it does have >0.15 fmols concentration of He on the re-extraction which is a positive result. The rest of the grains have a re-ext % of below 0.15% and as a result are likely inclusion free.

3.2 Uranium, Thorium, Samarium Concentrations

Table 2 shows the concentrations of U, Th and Sm in parts per trillion (ppt) measured by ICP-MS and Table 3 shows the single-grain ages for three out of our four samples. In these tables, "PtBk" samples are Pt blanks (empty Platinum crucibles) and "Bk" samples are non-Pt blanks. As previously stated, sample BH100/2 will not be included. The absence of significant concentrations of parent isotopes is the reason that the grains in this sample have anomalously low He concentrations and have to be discarded.

Grain BH101-2 has much lower U (37.56 ppm) and Th (7.90 ppm) concentrations compared to the grains BH101-4 (U=137.06 ppm, Th= 38.76ppm) and BH101-5(U=219.35 ppm, Th=70.30 ppm) (table 2). The geometry of the BH101-2 is not strikingly anhedral compared to the other grains in the sample (grain BH100-1 is very rounded and less ideally shaped than BH101-2), so grain shape was probably not a large factor in the difference in isotope concentrations (See appendix A for a Pax-it photos, grains geometries, measurements and descriptions).

Sample BH103 overall has low parent isotope concentrations (table 2). Grains BH103-1, BH103-2 and BH103-3 have relatively low U concentrations (24.35-39.38 ppt). All grains from sample BH103 have low Th (-3.31 ppt-11.41 ppt) and Sm (4.05 ppt-8.74 ppt) concentrations (Table 3); grain BH103-4 has a negative value for Th concentration which shows that the Th concentration in the grain is less even than the Th spike that was added for the isotope dilution.

Sample BH104 has very good reproducibility between the grain ages (Table 3). Grain BH104-1 has relatively high U (137.35 ppt) and Th (105.32 ppt) (Table 2) concentrations compared to the rest of the grains in the sample with the next highest values within the sample being 80.91 ppt of U and 36.66 ppt of Th. Grain BH104-5 on the other hand has a slightly lower U concentration (44.19 ppt) and significantly lower Th concentration (0.97 ppt) than the rest of the grains in the sample.

3.3 Grain Age Reproducibility

To evaluate the relevance of the ages of the remaining 12 grains, we look at the measurements reproducibility among the grains of each sample. All four grains from sample BH104 reproduce well; the oldest and youngest grains only have a 12% difference (7.03 Ma-7.91 Ma (table 3)). BH101 also reproduces relatively well except for grain BH101-2 which has a calculated age that is approximately twice that of the other 3 grains (BH101-2 is 13.83 Ma while the other 3 grains range from 5.62-7.75 Ma). Sample BH103 has variable reproducibility; two samples have similar ages (BH103-2 is 7.13 Ma and BH103-4 is 6.78 Ma) while the other two are significantly older and scattered (BH103-1 is 17.36 Ma and BH103-3 is 11.21 Ma) (Table 3).

To understand why some of our samples do not replicate well, one needs to consider several factors. One must consider the U, Th, Sm content (very high parent isotope concentrations will give more accurate ages), the Pt blanks (for contamination of U and Th), the $^{154}Sm/^{152}Sm$ and/or $^{238}U/^{235}U$ ratios (ratios close to the natural abundance show that the ages are probably accurate), the re-extraction percentages (high re-extractions reveal the presence of radioactive mineral inclusions) and the geometry of the grains (for the alpha-correction).

The concentrations of parent isotopes measured in the Pt blanks give a measure of how much U, Th and Sm could have been added through cross-contamination from the Pt crucibles that were used to pack the grains. The concentration of U in the crucibles is below 5% for all blanks (table 2) which shows that the crucibles do not interfere with U measurements for the samples (or do not contribute to any ^{238}U contamination). The Th contents measured in the Pt blanks however, are a problem. 3 of the 4 Pt blanks (ptbk1_r, ptbk2 and ptbk3) have concentrations of >10 ppm which is higher than some of our samples (Table 2). This, along with the fact that the procedural blanks (the non-Pt tube blanks, Bk1, Bk2 and Bk3) have significantly lower Th values, points to the fact that the excess Th is indeed coming from the Pt crucibles and not from other sources. The fact that some of our grains (BH101-2, BH103-3, BH103-4 and BH104-5) have lower Th concentrations, some over 50% less, than the Pt blanks shows that the Th contributions from the Pt tubes is highly variable and thus our error for Th measurements is quite large. $^{238}U/^{235}U$ ratios (Table 4) are a good indicator to test the quality of our measurements. If they are close to the natural abundance of Uranium, ~137.9 (Farley, 2002) then the dissolution of the grains likely was carried out fully and the age is probably good. In our case, only the samples with high U concentrations can be evaluated in this way because in samples with relatively low U concentrations, the concentration of ^{235}U will be below the sensitivity of the ICP-MS. Grains BH101-4, BH101-5 and BH104-1 all have high U content (137.06 ppm, 219.35 ppm and 173.35 ppm respectively (table 2)) and $^{238}U/^{235}U$ ratios close to the natural abundance which supports that the ages calculated for these grains are likely correct. The same test can be done with the ratio of $^{154}Sm/^{152}Sm$ (Table 4) (natural abundance: ~0.85 (Ramamoorthy et al., 2002)). Most of our grains with

relatively high Sm concentrations (greater than ~20 ppt) show a ratio close to the natural abundance (within ~5%). All of sample BH101 (46.75 ppt-88.25 ppt) along with grains BH104-1 (23.22 ppt) and BH104-2 (42.66 ppt) have high Sm concentrations (table 2) and ratios very near the natural abundance (0.85-0.88) (table 4). This supports that these grains will probably yield reliable ages.

3.4 Limitations of the AHe Dating Method

While the AHe dating method has been proven accurate for calculating the cooling ages of select minerals in the shallow crust (Farley, 2000, Farley et al., 2002 and references therein), there are some limitations to the method that we have come across during this study. It is possible that if a more powerful microscope had been used, the nature of some of the tiny inclusions within our samples could have been detected, along with smaller cracks and fractures that may have contributed to an increase in diffusion of He. The mineral inclusions potentially present within our samples were too small to be formally identified so it was difficult to determine if they were α-particle contributors, such as zircon, monazite, xenotime, or harmless silicate minerals.

The Pt crucibles that were used to house the apatites during He extraction and shipping have posed a certain number of problems to the ICP-MS operator (M.G. Fellin) who processed our samples for U-Th-Sm concentrations measurements. She first tested her dissolution technique on one of the Durango apatite standards that was sent with our samples. The full dissolution of the sample failed and anomalously low U-Th-Sm concentrations and a non-standard U-Th ratio were reported; this occurred also on a second attempt on another Durango standard which was let to dissolve longer with higher but still anomalously low parent isotope concentrations. This procedure involves

dissolving the apatites while they are still sealed inside the Pt crucibles; this procedure is routinely adopted because, in general, the Pt tubes are quite difficult to close completely and the acid mix will most of the time find its way to enter the Pt foil and dissolve the grain packed into it. This was not the case with our samples, the size of the openings in the tube were so small that even after ~24 hours of dissolution, complete dissolution was not guaranteed in our samples. It is likely that our Pt foils were sealed too tightly during packing. The obvious solution to this would be to increase the concentration of the acids used for dissolution and/or the dissolution time so that the entire Pt tube would also dissolve with the grain. However, dissolution of the Pt tubes should not be done because when Pt is dissolved into the solution, it interferes with the measurements of ^{235}U and ^{238}U in the mass spectrometer. The Pt reacts with the ionized Ar plasma used in the ICP-MS to form PtAr molecules. Ar has an atomic mass of ~40 amu and the most common Pt isotopes are ^{194}Pt, ^{195}Pt, ^{196}Pt and ^{198}Pt. When ^{195}Pt and ^{198}Pt react with the ^{40}Ar, they create PtAr molecules with masses of 235 amu and 238 amu respectively; due to the similarity of the atomic masses of these PtAr molecules and U isotopes, they can be mistakenly identified in the ICP-MS. A possible solution to this issue that is in use at other labs is to use niobium crucibles instead of Pt and dissolve both the grain and crucible together. This would eliminate the possibility of creating PtAr molecules with the same atomic mass as uranium elements. Since Nb has a much smaller mass than Pt (~93 amu for Nb versus ~195 amu for Pt), any molecules made will be far lighter than U, so this mass contamination will not occur.

There is another limitation however that arises from dissolving the crucible itself. If the entire crucible is dissolved (either the Pt or Nb crucible), there will be 1-2 mg of

dissolved metals in the resulting solution. This solution is then dried until the HNO_3 is concentrated at ~1%, which leaves a final volume for the solution of ~1ml. With a volume this small, the 1-2 mg of metal becomes concentrated at 1000-2000 ppm. Processing this solution will be essentially coating the ICP-MS with metal. This is not a problem if the ICP-MS is exclusively used for U-Th-Sm measurements, but problems could arise when measuring other elements as the Nb or Pt could react with these elements and skew the results (M.G. Fellin, personal communication).

3.5 Comparing AHe ages to existing AFT ages

Comparing the ages obtained from our samples to previously published Apatite fission-track ages (Table 3.5) on the same samples (Grujic et al., 2006), indicate that our AHe ages are younger but not by a large amount. Sample BH104 has the smallest range between AHe and AFT dates; the sample has an AFT date of 8.6±0.6 Ma while the AHe ages for our grains range from 7.03 Ma to 7.91 Ma. BH103 has two outliers (BH103-1 at 17.36 Ma and BH103-3 at 11.21 Ma) with very large ages that do not correlate with the AFT age of 7.8±0.7 Ma. The other two ages, 7.13 Ma and 6.78 Ma are fairly close but once again they are younger. The AFT age for BH101 (6.1±0.6 Ma) is younger than the average AHe age for the same sample (6.8±0.22 Ma); this is impossible due to the T_c of the AHe system (~75°C) being lower than that of the AFT system (~120°C). How this may have occurred is discussed in the following section

3.6 Interpretation of Ages

From the original 16 grains that were sampled in this study 9 grains were finally chosen for use in constructing an age-elevation profile, which will be discussed later. The 7 grains that were not used (3.1-3.3) were discarded for several reasons. First, as previously

stated, the entirety of sample BH100/2 was discarded due to anomalously low parent isotope values, so no ages were calculated for these grains. The other three grains, BH101-2, BH103-1 and BH103-3, yielded anomalously high ages so they were discarded as outliers. Sample BH103-1 returned an age of 17.36±0.63 Ma and is the largest outlier; it is over twice the age of the lowest 2 samples in the group (6.78±0.3 Ma and 7.13±0.26 Ma). BH103-3 returned an age of 11.21±0.39 Ma which is much lower than BH103-3 but still considerably higher than the lowest two samples; those two samples (BH103-2 and BH103-4) have the best agreement of ages within the sample. BH101-2 returned an age of 13.38±0.48 Ma which is considerably older than the other 3 grains in the sample (5.62±0.19 Ma, 7.02±0.22 Ma and 7.75±0.24 Ma). The grains actually chosen have a range of 5.62±0.19 Ma to 7.91±0.25 Ma.

The exclusion of the three grains due to high ages leaves 2 of our samples with fewer grains than the original four, which may really decrease the accuracy and relevance of the mean ages calculated. Sample BH103 has only two grains remaining after the exclusion of BH103-1 and BH103-3, thus the mean age calculated only reflects 2 data points. To avoid the problem of having to exclude such a high proportion of grains in the future, a large sample of grains, probably about 10 grains per sample, should be collected and analyzed. This is less of a problem with samples BH101 and BH104 which have 3 and 4 grains left respectively, but more grains is always better.

When comparing the mean ages obtained from these samples using the AHe method to the mean ages obtained from the same grains using the AFT method, it is evident that there is no simple correlation between the two. The oldest samples, BH103 and BH104, both returned a younger age using AHe than AFT; sample BH101 however returned an

identical (within error) to the AFT older age using AHe (6.8±0.2 for AHe and 6.1±0.6 for AFT). The AHe closure temperature is ~70°C while the AFT system closes at ~120°C; this means that the cooling age obtained from a given sample using AHe must be younger than the cooling age obtained from the same sample using AFT. When this does not occur, there must be some sort of bias that leads the AHe age to be older (or the AFT age to be younger) than it really is.

AHe ages that are older than AFT ages for the same sample have been encountered in a number of studies (e.g. Green et al., 2006, Biswas et al., 2007). Several explanations have been put forward as how it is possible for such biases to occur within the AHe system. Hendricks and Redfield (2005) suggested that anomalous fission track behavior (such as radiation enhanced annealing), at low temperatures due to non-thermal processes (i.e. radioactive decay), may be to blame for this problem. This is probably not an issue in our case because their experiments took place within a craton which exhumes at a much slower rate than active mountain belts; our samples probably make it to the surface too fast for this annealing to accumulate. Green et al, (2006) however present data from a range of geologic settings that show that instead of anomalous fission track behavior, accumulated radiation damage which results in a change in the He retention properties of apatite, may be to blame. This damage is the product of successive alpha decay and spontaneous fission; both of these reactions release high energy particles that damage the crystal lattice. While the exact mechanism of this effect is not currently known, it has been shown that the effect increases significantly as AFT ages increase (Green et al., 2006). As AFT ages increase, so must the resulting radiation damage to the lattice; apatites with very high U and/or Th concentrations would also contribute to a higher rate

and concentration of radiation damage due to the increased number of alpha decays and fission events. Because of this effect, ages based on the general diffusion behavior apatite are only valid if accumulated radiation dose is similar to that of the Durango apatite, or some other standard whose diffusion behavior has been extensively studied; in general, based on a typical basement apatite with U and Th contents of ~10 ppm and ~30 ppm respectively, AFT ages of ~100 Ma is the theoretical upper limit of validity of published diffusion behavior in apatite (Green et al., 2006). While our samples are much younger than 100 Ma, it is still possible that this radiation damage has some sort of effect on the ages of our grains.

Biswas et al., (2007) obtained several AHe ages that were older than the AFT ages obtained from the corresponding samples. They also attributed this anomaly to probably radiation damage within the apatite, given high parent nuclide concentrations. Figure 3.1 shows that with an increasing trend of effective uranium concentrations, AHe ages increase accordingly. Also, they surmised that the similarity of their AHe and AFT ages could be due to the shift (increase) of the AHe system closure temperature in response to the increased He retentivity caused by radiation damage in their Uranium and Thorium-rich apatite.

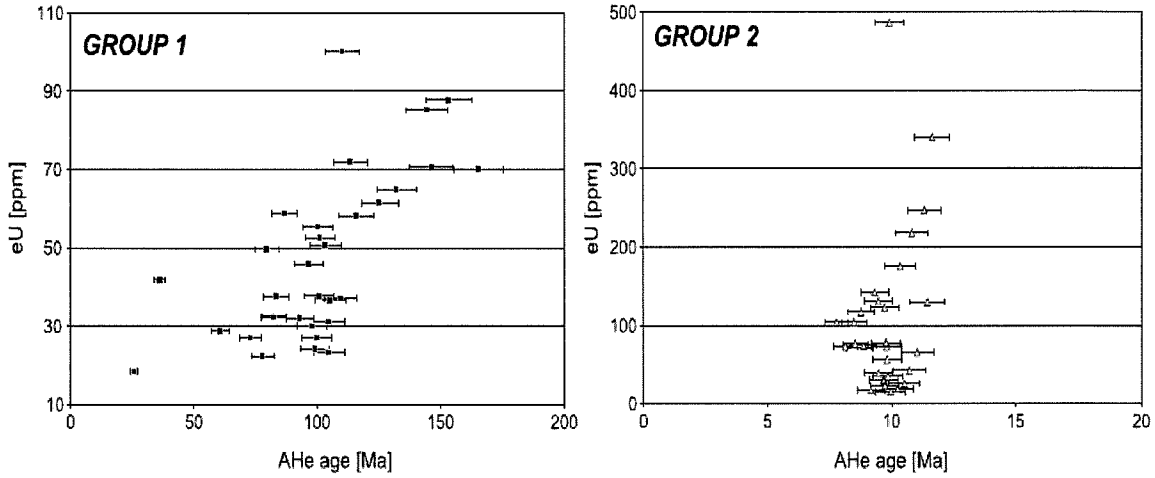

Figure 3.1: AHe ages versus effective uranium concentration. The correlation in group 1 shows an obvious positive trend of increasing calculated age with increasing effective uranium. This exemplifies the expected positive correlation between He retentively (using AHe age as a proxy) and radiation damage (using effective uranium as a proxy). Group 2 does not show this correlation and was interpreted to have cooled from ~90°C, which is the critical temperature above which radiation damage becomes negligible due to annealing. (Biswas et al., 2007 and references therein).

One of the things that can be learned by comparing AHe and AFT ages is the cooling rate between both ages. By looking at a set of closure temperatures and the amount of time it took a mineral to move between them, the cooling rate of that mineral can be obtained. If we do this for our grains, we obtain following cooling rates (using an AHe T_c of ~75°C and AFT T_c of ~120°C obtained from figure 3.2): a cooling rate of ~50.0°C/Ma between ~7.8Ma and ~7.0Ma and a cooling rate of ~33.3°C/Ma between ~8.6Ma and ~7.4Ma. A cooling rate cannot be calculated for sample BH101 due to the AHe age being older than the AFT age. This would reflect a heating rate rather than a cooling rate, which is meaningless in this case due to the theoretical impossibility of AHe ages being older than AFT ages.

3.7 Cooling Rates

As previously stated, the ages obtained for our samples are in fact the time since the samples have last cooled through the effective closure temperature of the AHe system. This is ~75°C determined from the calculated cooling rate between our AHe and AFT ages and then graphically deduced from figure 3.2. Cooling rate is calculated using equation 3.1:

$$\mathbf{DT/dt = Cooling\ Rate\ (in\ °C/Ma)} \qquad (3.1)$$

where DT is the change in temperature over the time between the sample ages in the AHe and AFT thermochronometric systems, and dt is the difference in ages of the samples . DT is assumed to be constant at ~40°C based on the specifications used in Reiners et al., (2006) (Fig. 3.2). One of our samples (BH101) predicted a negative cooling rate so it was not used in the calculation; as a result the cooling rate is only known from the period of 7.96-8.60 Ma. An average cooling rate of ~40°C/Myr was calculated for this period.

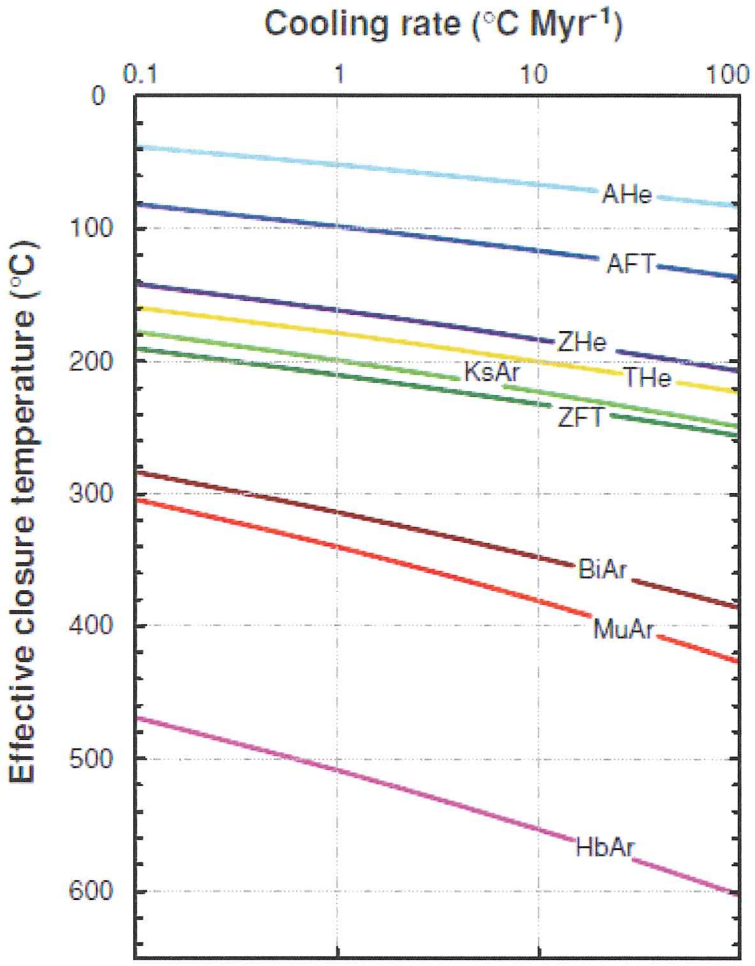

Figure 3.2: Shows the effective closure temperature for a range of He, fission track and Ar thermochronometers as a function of cooling rate. Note the temperature range between the T_c of the AHe and AFT systems only slightly increases over a four orders of magnitude increase in cooling rate. (Reiners and Brandon, 2006).

3.8 Exhumation rates

The purpose of our study is to constraint exhumation rates within this orogenic segment of the Bhutan Himalaya. Exhumation represents the displacement of rocks with respect to the surface (England and Molnar, 1990). In contractional settings, the rate of exhumation is the rate of removal of overburden crustal section and can be approximated as being the erosion rate (Fig. 3.3)

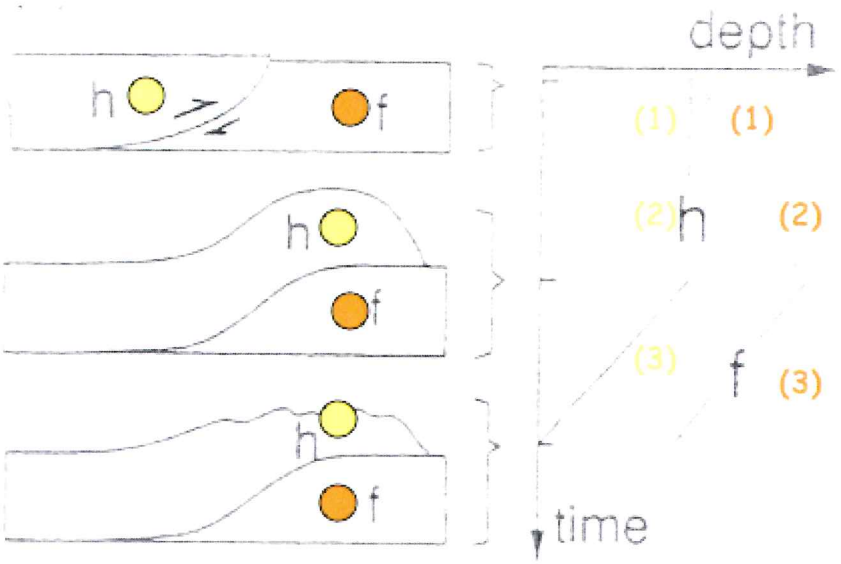

Figure 3.3: Cartoon model representing 3 steps in the transportation of our samples: 1) horizontal shortening, 2) crustal thickening and 3) erosion and of the crust and subsequent exhumation of the sample. The accompanying graph shows the depth of the sample (yellow dot) on the hanging wall (h) over time compared to a static point (orange dot) on the footwall (f). Time ends when the yellow dot is exhumed to surface (Stüwe and Barr, 1999).

In order to extract exhumation rates from our cooling rates, we can use 2 approaches: (1) convert dT into dz. Dz is the distance that the sample has travelled since passing through the closure temperature of a given thermochronometric system. In the simplest case, this distance can be determined by using a constant geothermal gradient (this approach can a priori be used when the modern geothermal gradient has been empirically calculated from heat flow measurements from boreholes and assuming that it did not change since the time our crustal section was exhumed) or by calculating a steady-state one-dimensional vertical profile for our crustal section (beyond the scope of this work). Assuming vertical sample exhumation, the exhumation is calculated by measuring the distance from the surface (where the sample was collected) to the closure temperature (this is dz) and divide it by the sample age (e.g. Whipp and Ehlers, 2007).

In active orogens, however, the thermal field is multidimensional and commonly transient (eg. Ehlers and Farley., 2003) – taking into account these facts would require the using 3-D thermal-kinematic modeling which is well beyond the scope of this study. The common values adopted for geothermal gradients in orogenic context oscillate between 25-35°C/km (but it can be much higher when erosion is fast and advects shallow isotherms toward the surface). Fully aware of the limitations of this approach (we are using an assumed constant thermal gradient which in reality needs to be exactly calculated through thermal modeling or borehole measurements), we calculate exhumation rates assuming a steady geothermal gradient of 25-35°C/km. For this range of the geothermal gradient, closure temperature that was determined previously (75°C) and a mean surface temperature of 5-15°C (samples elevation between 1500-3500 m at temperate climate latitude), dz was calculated to be 1.7-2.8 km. By dividing dz by the sample age, exhumation rates of 0.25-41 mm/yr for sample BH101, 0.24-0.40 mm/yr for sample BH103 and 0.23-0.38mm/year for sample BH104. These exhumation rates are considerably lower than the ones obtained from the vertical profile. This is so because the exhumation rates obtained from this method are average rates between the age of the sample and the present day.

(2) A second approach involves the construction of a vertical profile (e.g. Fig. 3.4). In areas of assumed constant exhumation, cooling ages reach a steady state in which they plot linearly on a graph of cooling age against depth; this is known as an age-elevation profile (Ehlers et al., 2003). Since on a large scale, thermal isotherms mimic the above topography (Fig. 3.5), it is difficult to measure exhumation directly without hitting some limitations and making large assumptions (such as pure vertical exhumation).

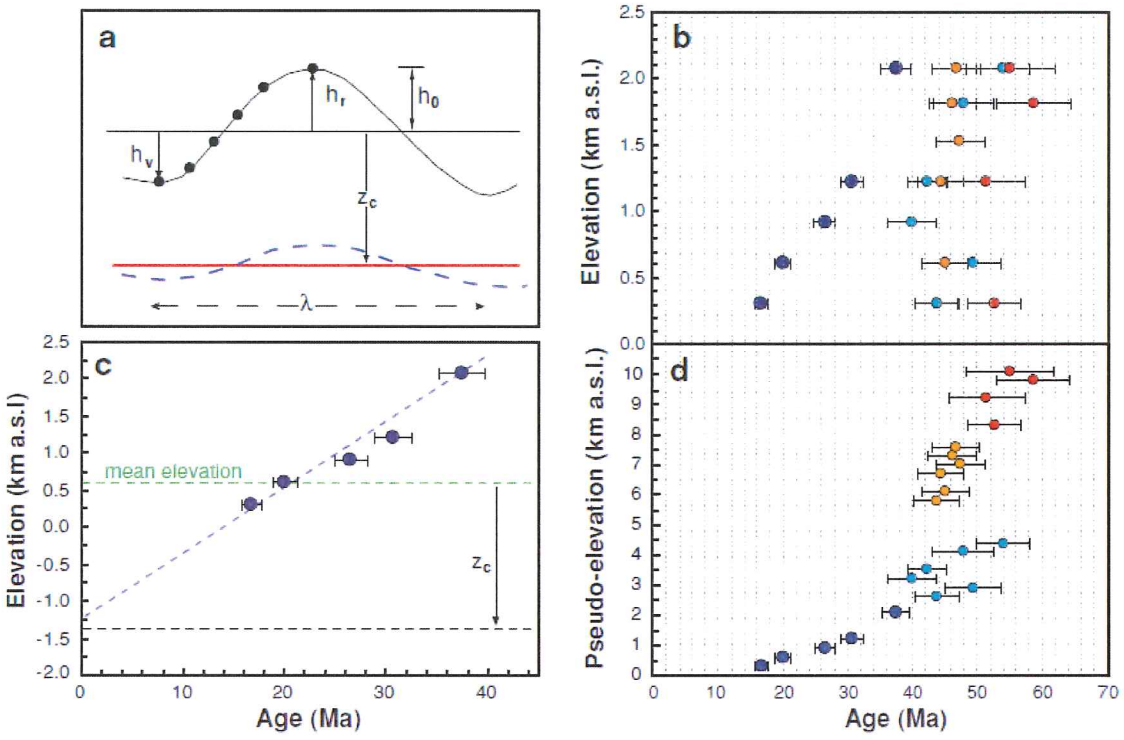

Figure 3.4: Four graphs that illustrate concepts within and examples of thermochronologic vertical profiles. 9a shows how a vertical transect should be sampled, from the bottom of a valley to the top of a ridge (if a vertical cliff section is not available). It also shows that the degree of the deflection of the isotherms is based on the wavelength of the undulations of topography (λ) and that these topographic effects will change the depth of the closure isotherm (Z_c). This model assumed vertical exhumation. 9b shows ZFT (red dots), ZHe (orange), AFT (light blue), and AHe (dark blue) ages for samples from a vertical transect with 1.8 km of relief, collected over ~7 km horizontal distance, on Mt. Hefty, southeastern Alaska. 9c shows that the slope of the best-fit line of AHe ages gives the average erosion rate (in our case exhumation rate) by using Z_c/τ_m. Z_c represents the depth of the closure isotherm while τ_m represents the time at which the sample passed through that isotherm. 9d is a stacked vertical profile that we will not be using in our study. (Reiners and Brandon, 2006 and references therein)

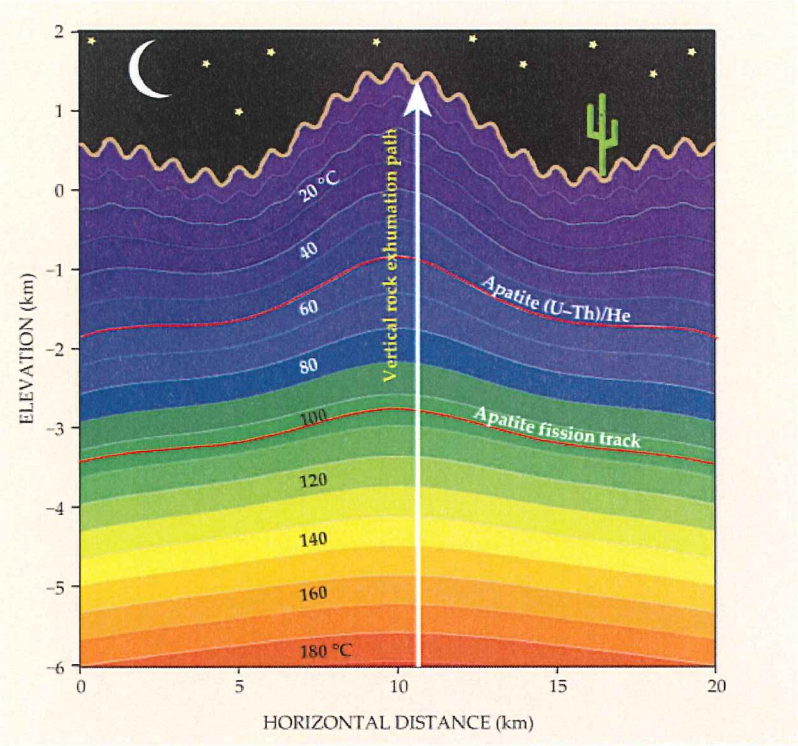

Figure 3.5: A graphical representation of how isotherms might be deflected by topography and the degree of similarity between them depending on depth. From the approximate depth of AHe closure to the surface, the thermal isotherms follow nearly parallel to the long wavelength undulations of surface topography. (Reiners et al., 2009)

There are however, several limitations to this simple 1-dimensional model of exhumation. For this model to be accurate, some assumptions must be made (eg. Huntington et al., 2007): 1) particle path must be essentially vertical because isotherms are assumed to be horizontal and 1-dimensional with no lateral component of movement; 2) regional topography must have been in near steady-state condition during the period of exhumation (Braun, 2002) because as shown above (Figs. 3.4 and 3.5), topography has an influence on the thermal structure of the crust by deflecting the isotherms

Simple 1-dimentional exhumation is likely not the case in most, if not all, orogens; Tectonics forces driving thrusting, surface erosive processes such as precipitation

distribution, river incision, glacial erosion and land sliding, likely result in exhumation vectors in 2, or more likely, 3 dimensions.

Furthermore, the isotherms within an orogen, especially one as tectonically and erosively active as the Himalayas, are also not likely to be horizontal (Huntington, 2007). Long and short range undulations and deflections of the isotherms can be caused by topographic features, deflection of isotherms during thrust faulting and advection of isotherms under focused and vigorous erosion. Although the effects of topography on isotherms do decrease significantly with depth (Huntington et al., 2007 and references therein), the AHe method focuses on exhumation in the shallow crust. As such, a large portion of the time spent during exhumation will likely be spent moving through topographically skewed isotherms. Local spatial variations in the thermal gradient are caused by valleys and ridges (Huntington et al., 2007); the severity of this effect depends on the wavelength of topographic valleys and ridges, the relief between these valleys and ridges and also on the exhumation rate. The faster the exhumation rate, the greater the compression of the isotherms will be, and vice versa. Denudation also plays a role in changing the shape of isotherms; advection of warmer rocks towards the surface cause isotherms to shallow and subsequently cause the thermal gradient to increase (Huntington et al., 2007).

The orientation of the sampling profile with respect the overall exhumation vector is another limitation when 1-D vertical exhumation does not occur (Fig. 3.6). Our profile, which is oriented ~45° to the movement on the main thrust fault driving exhumation in the late Miocene (E-W trending Main Boundary Thrust and subsequently in the late Pliocene the Main Frontal Thrust (Fig. 1.1) falls somewhere between figures 3.6c and

3.6d. This composite orientation makes it difficult to determine what kind of effect this will have on our ages.

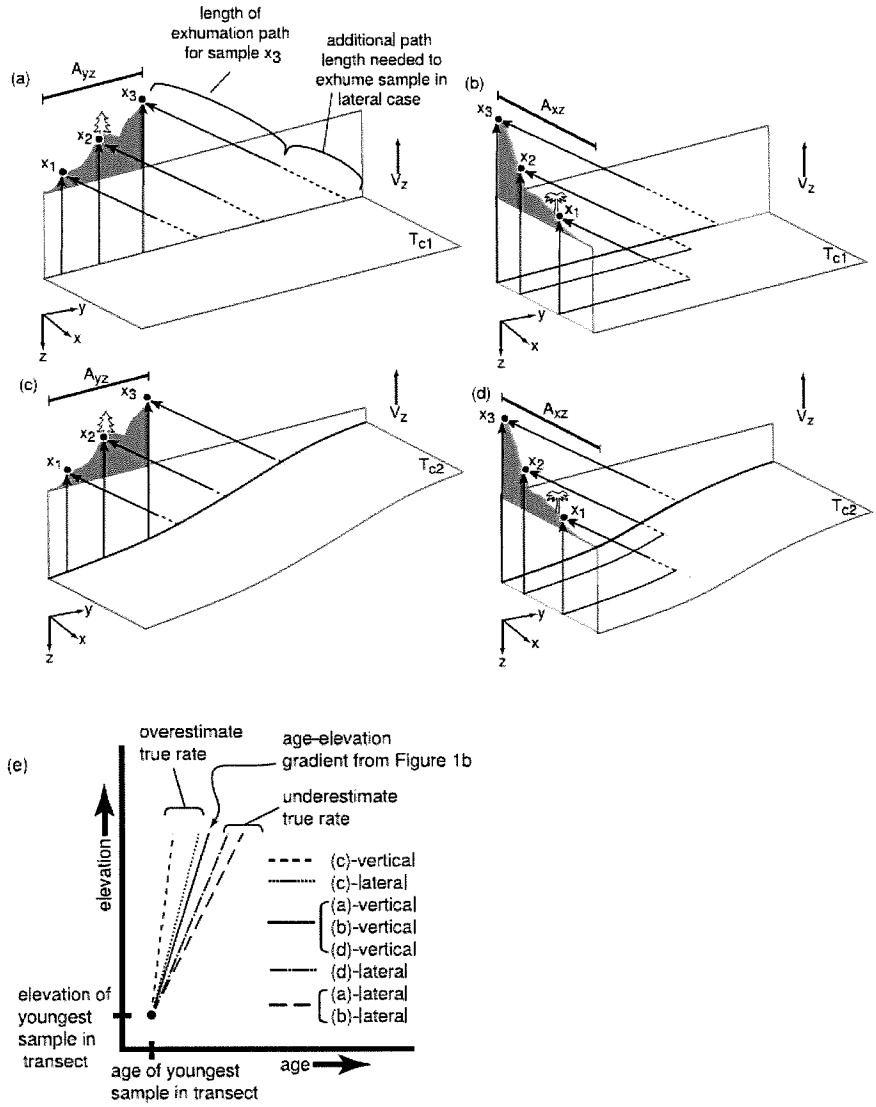

Figure 3.6: Sample distribution and corresponding age-elevation profile. 3.6a-3.6d show the particle paths during exhumation along 4 differently oriented elevation profiles: two profiles 90° to each other on a flat closure isotherm (3.6a and 3.6b) and one each parallel and perpendicular to a fault ramp structure with a non-flat closure isotherm (3.6c and 3.6d). Black arrows depict exhumation vector. All four models were done twice, once with lateral displacement and one with vertical. The summary of cooling ages with respect to elevation is shown in diagram 3.6e (Huntington et al., 2007).

Using our measurements of cooling ages and knowledge of the sample elevations, an age-elevation profile was constructed for our data set (Fig. 3.7). AFT ages for the same samples are also plotted on this profile (Grujic et al., 2006).

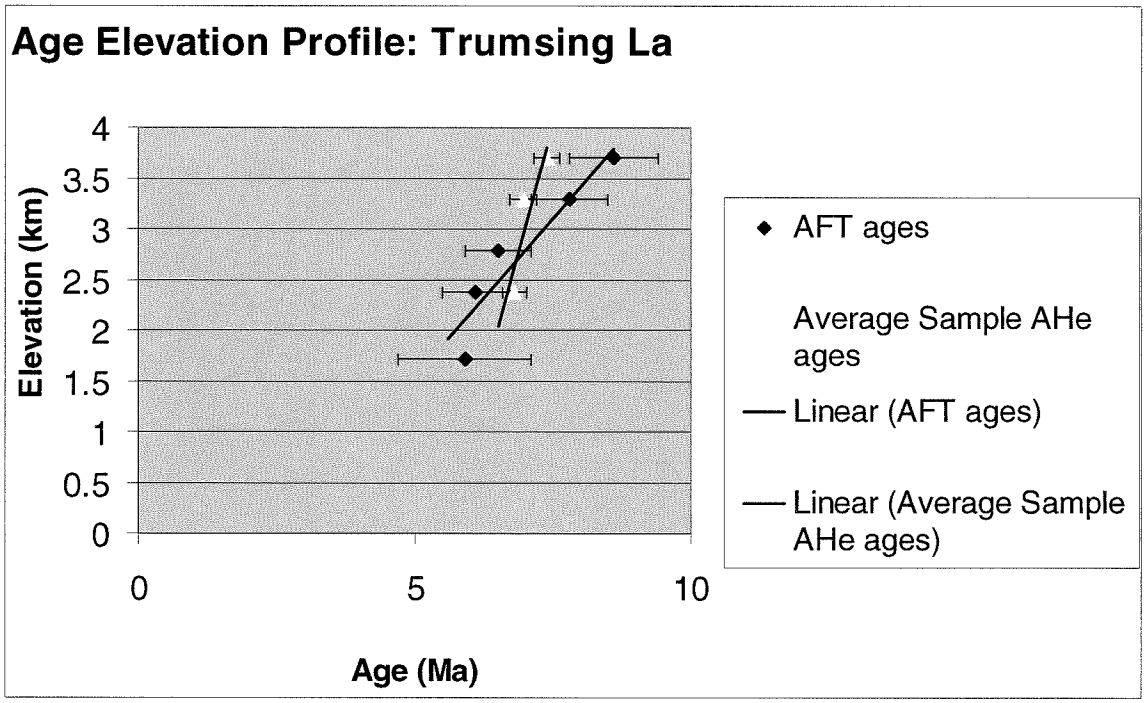

Figure 3.7: Age-elevation profile for AHe and AFT ages. Yellow data points represent the statistical mean of the grain ages obtained for each sample. Blue points represent AFT ages for our samples, along with two other samples from the sample profile (BH100/2, which we discarded, and BH102, which was not analyzed). A line of best fit is passed through the average AHe and AFT ages where the slope of the lines indicate the average apparent exhumation rate over the time period sampled.

It is immediately visible from figure 3.7, that the AHe data has a much steeper slope, and therefore a much higher exhumation rate (~1.9mm/yr), than the average rate from the AFT data (~0.6mm/yr). The He data shows a faster exhumation rate between 6.8-7.4 Ma which is different than the AFT derived exhumation rate for the same period. Looking at the AFT ages, the average exhumation rate does not fit the entire data series very well. It looks like there may be a change in exhumation rate at ~6.5 Ma as indicated by the break in slope at that time (this was initially suggested in Grujic et al., 2006). If a line is fit to

only AFT samples, BH100/2, BH101 and BH102, the resulting slope, 1.68 mm/yr, is similar to the slope of the AHe line, 1.9 mm/yr, although the timing does not fit perfectly (Fig. 3.8). This may signify a true increase in exhumation somewhere between 6-7 Ma, however, as previously noted, our ages may not be accurate due to the small amount of grains taken for each sample, and other limitations previously stated for the low temperature AHe method.

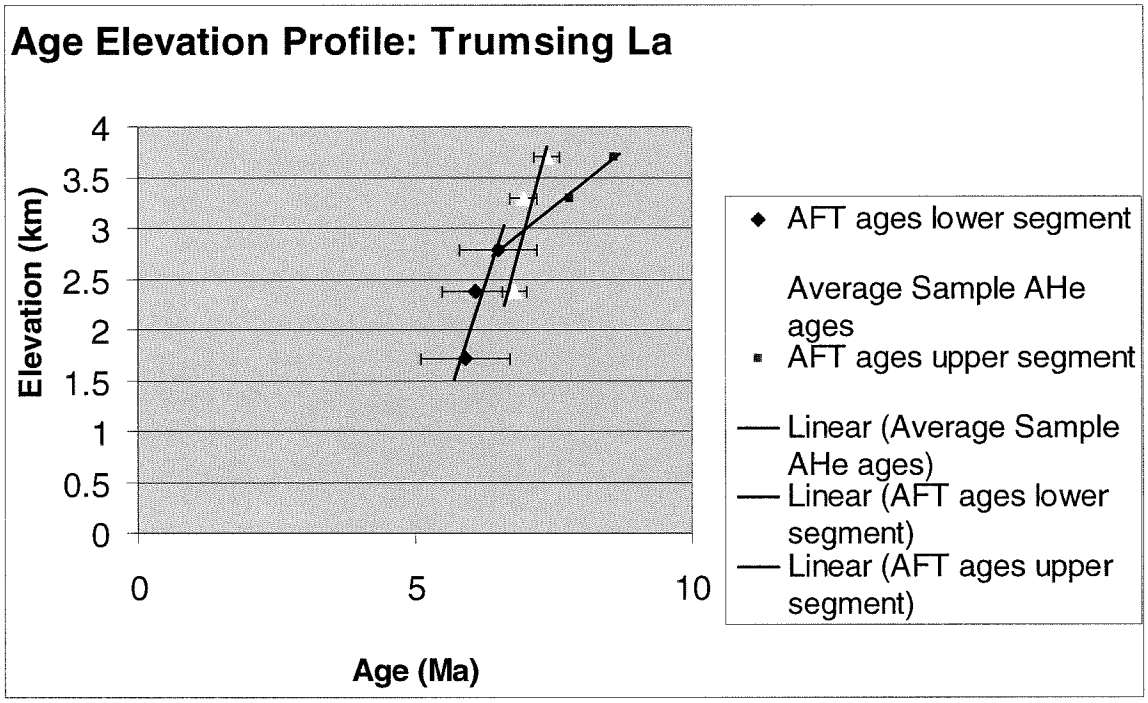

Figure 3.8: The same data as figure 3.7 the AFT data is broken into two slopes converging on Sample BH102. The two trend lines fit the AFT ages much more accurately than a single one did. Note now how the slopes of the lower AFT data and AHe data are nearly parallel.

These two slopes, while different, are in better agreement than the AHe data was with the single step AFT exhumation rate. This indicates two different exhumation rates for the same time period, which is impossible. A potential explanation for these different slopes is that the slope is artificially increased for the shallower thermochronometer (He)

because the shallow subsurface isotherms are more deflected and compressed by overlying topography and/or upward advection and consequently, at shallower depths, samples have to travel less to cool a certain dT than they have to from deeper depths to cool by the same dT.

Chapter 4-Conclusion

From AHe cooling ages we obtained from our apatites, and the subsequent exhumation rates obtained from our constructed age-elevation profile, we can infer that between ~6.8 - 7.4 Ma the exhumation rate between He and AFT are different. Sample BH101 does however pose a problem; the AHe age of this sample is older than the AFT age, which cannot be. Nonetheless, this sample was included in the age-elevation profile because we already have a relatively small amount of data points. It is likely that our exhumation rate has been artificially increased due to our He thermochronometer's sensitivity to the deflection of shallow isotherms by overlying topography. Most likely sample BH101 biases significantly the slope value, and hence leads to an overestimate the He exhumation rate.

If we just look at the last 3 AFT ages, BH100/2, BH101 and BH102, and draw a new trend line through them, then a break in slope in the AFT AERs is clearly observable (and was already documented by Grujic et al., 2006). It indicates an increase in exhumation rates at point BH102 from 0.43mm/Ma to 1.6 mm/Ma. Calculating exhumation rates using the Dz method (Chpt. 3), the rates are much lower (0.025-0.054 mm/yr), this indicates that these rapid exhumation rates documented between AFT samples BH102 and BH100/2 were not sustained until the present; exhumation had to slow down between point 1and the present.

In future studies, to get better age control on our samples, more grains per sample need to be analyzed; an average age from a suite of 10-12 grains would be much more meaningful than the ages obtained from the 2-4 grains per sample we use in this study.

More samples in general need to be included to get a more accurate representation of the exhumation rate in the Pliocene, also to get younger ages, samples collected at lower elevation are required; we did not have those in hand for this study. . Right now we use only three samples to graphically calculate exhumation rates using an age-elevation profile; if we had more samples, the slope of their ages as a function of elevation might be more accurately constrained.

The most useful numerical results of this study provide refined exhumation rates for the late Miocene-Pliocene transition. We were not able to constrain erosion rates tor the Pliocene period of time because AHe ages we obtained were unexpectedly old.

Empirically, the results of this study will also help us refine our sample strategy for future attempts to tackle the question posed at the beginning of this study; whether local variations in precipitation volume and intensity would have led to an increase or decrease in erosion rates.

References

Beaumont C., Jamieson R.A., Nguyen R.H., Lee B. Himalayan tectonics explained by extrusion of a low-viscosity crustal channel coupled to focused surface denudation, 2001. Nature; v. 414.

Biswas, S., Coutand, I., Grujic, D., Häger, C.; Stockli, D., Grasemann, B. Exhumation and uplift of the Shillong Plateau and its influence on the eastern Himalayas: New constraints from apatite and zircon (U-Th-[Sm])/He and apatite fission track analysis, 2007. Tectonics; v.26.

Bookhagen B., Thiede R., Strecker M. Late Quaternary intensified monsoon phases control landscape evolution in the northwest Himalaya, 2005. Geology; v. 33; i. 2; p. 149-152.

Bookhagen, Bodo; Burbank, Douglas. Topography, relief, and TRMM-derived rainfall variations along the Himalaya, 2006. Geophysical Research Letters 33.

Braun J. Quantifying the effect of recent relief changes on Age-elevation relationships, 2002. Earth and Planetary Science Letters; v. 200; p.331-343.

Daniel, J. Exhumation of the Main Central Thrust from lower crustal depths, eastern Bhutan Himalaya, 2003. Metamorphic Geology.

Duncan C., Masek J., Fielding E. How steep are the Himalaya? Characteristics and implications of along-strike topographic variations, 2003. Geology, v. 31; no. 1; p. 75–78.

Ehlers T.A., Farley K. A. Apatite (U–Th)/He thermochronometry: methods and applications to problems in tectonic and surface processes, 2003. Earth and Planetary Science Letters; v. 206; i. 1-2; p. 1-14.

England P., Molnar P. Surface uplift, uplift of rocks, and exhumation of rocks, 1990. Geology; v.18; p.1173–77.

Farley K., Stockli D. (U-Th)/He Dating of Phosphates: Apatite, Monazite and Xenotime, 2000. Reviews in Mineralogy and Geochemistry; v. 48; i. 1; p. 559-577.

Farley, Kenneth. (U-Th)/He Dating: Techniques, Calibrations, and Applications, 2002. Reviews in Mineralogy and Geochemistry; v. 47; i. 1; p. 819-844.

Gansser, A., 1983, Geology of the Bhutan Himalaya: Stuttgart, Birkhäuser Verlag, 181 p.

Google Earth image

Green P., Crowhurst P., Duddy I., Japsen P., Holdford S. Conflicting (U-Th)/He and fisson track ages in apatite: Enhanced He retention, not anomalous annealing behavior, 2006. Earth and Planetary Science Letters; v.250; p.407-427.

Grujic D., Coutand I., Bookhagen B., Bonnet S., Blythe A., Duncan C., 2006. Climatic forcing of erosion, landscape, and tectonics in the Bhutan Himalayas; Geology; v.34; p.801–804.

Grujic D., Hollister L.S., Parrish R.R. Himalayan metamorphic sequence as an orogenic channel: Insight from Bhutan, 2002. Earth and Planetary Science Letters; v. 198; p. 177–191.

Hendriks B., Redfield T. Apatite fission track and (U–Th)/He data from Fennoscandinavia: an example of underestimation of fission track annealing in apatite, 2005. Earth and Planetary Science Letters; v.236; p. 443–458.

Harris, N. The elevation history of the Tibetan Plateau and its implications for the Asian Monsoon, 2006. Palaeogeography, Palaeoclimatology, Palaeoecology; v. 241; p.4-15.

Hodges, K.V. Tectonics of the Himalaya and southern Tibet from two perspectives, 2000. Geological Society of America Bulletin; v.112; p. 324-350.

Huntington K. W., Ehlers T.A., Hodges K.V., Whipp Jr D.M. Topography, exhumation pathway, age uncertainties, and the interpretation of thermochronometer data, 2007. Tectonics; v.26.

Kellet D. A., Grujic D., Erdmann S. Miocene structural reorganisation of the South Tibetan detachment, eastern Himalaya: Implications for continental collision, 2009. Lithosphere; v.1; no.5; p.259-281.

MacQuarie University website. http://www.eps.mq.edu.au/USRG/facil.html

Molnar, P. Late Cenozoic Increase in Accumulation Rates of Terrestrial Sediment: How Might Climate Change Have Affected Erosion Rates? 2004. Annual Review, Earth and Planet Sciences; v.32; p.67–89.

Patriat P., Achache J. India-Eurasia collision chronology has implications for crustal shortening and driving mechanism of plates, 1984. Nature; v. 311, i. 5987, p. 615-621.

Ramamoorthy N., Saraswathy P., Das M.K., Mehra K.S., Ananthakrishnan M. Production logistics and radionuclidic purity aspects of 153Sm for radionuclide therapy, 2002. Nuclear Medicine Communications; v. 23; i. 1; p. 83-89.

Ramstein G., Fluteau F., Besse J. Effect of orogeny, plate motion and land-sea distribution on Eurasian climate change over the past 30 million years, 1997. Nature; v. 386; p. 788–795.

Raymo M.E., Ruddiman W.F. Tectonic forcing of late Cenozoic climate change, 1992. Nature; v.359; p.117–122.

Reiners P. W., Brandon M. T. Using Thermochronology to Understand Orogenic Erosion, 2006. Annual Review of Earth and Planetary Sciences; v. 34; p. 419-466.

Reiners P. W., Shuster, D. L. Thermochronology and Landscape Evolution, 2009. Physics Today. v. 62; i. 9; p. 31-36.

Thiede R. C., Arrowsmith J. R., Bookhagen B., McWilliams M. O., Sobel E. R., Strecker M. R. From tectonically to erosionally controlled development of the Himalayan orogen, 2005. Geology; v.33; no.8; p. 689-692.

Whipp D.M. Jr., Ehlers T.A. Influence of groundwater flow on thermochronometer-derived exhumation rates in the central Nepalese Himalaya, 2007. Geology; v. 35; i. 9; p. 851-854.

Whipple, K. X. "The Influance of climate on the tectonic evolution of mountain belts." Nature Geoscience; v.2; 2009.

Wobus, C.; Heimsath, A.; Whipple, K.; Hodges, K. Active out-of-sequence thrust faulting in the central Nepalese Himalaya. Nature; v.434; p.1008–1011; 2005.

A. Appendix A

Sample BH100/2 - Grain #1

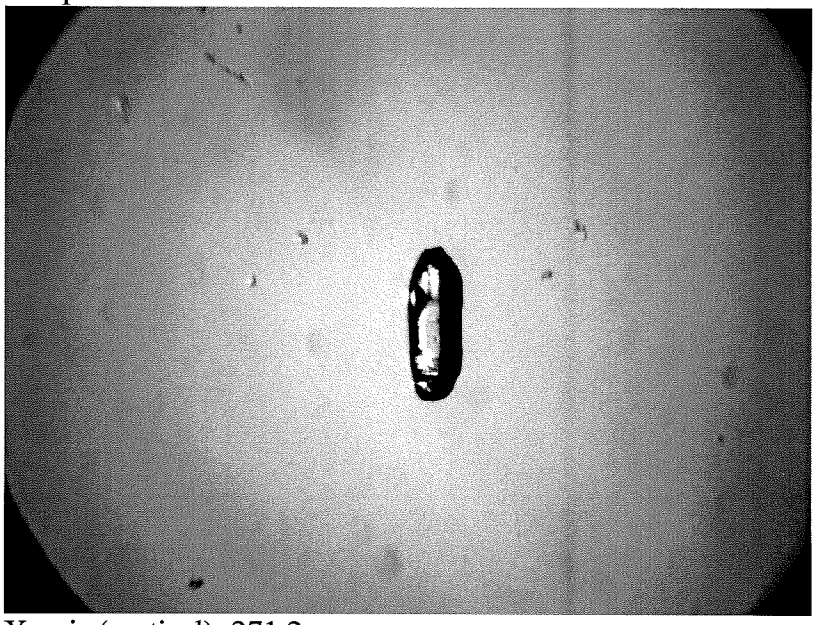

X-axis (vertical): 271.2μm
Y-axis (Horizontal): 94.4 μm

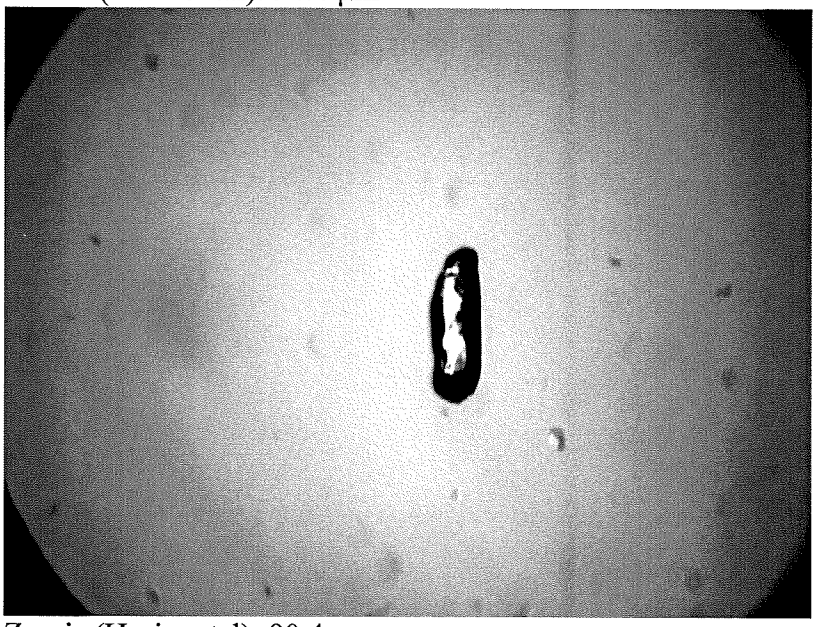

Z-axis (Horizontal): 90.4 μm

Description: No inclusions, slightly eroded surface with rounded ends.

Sample BH100/2 - Grain #2

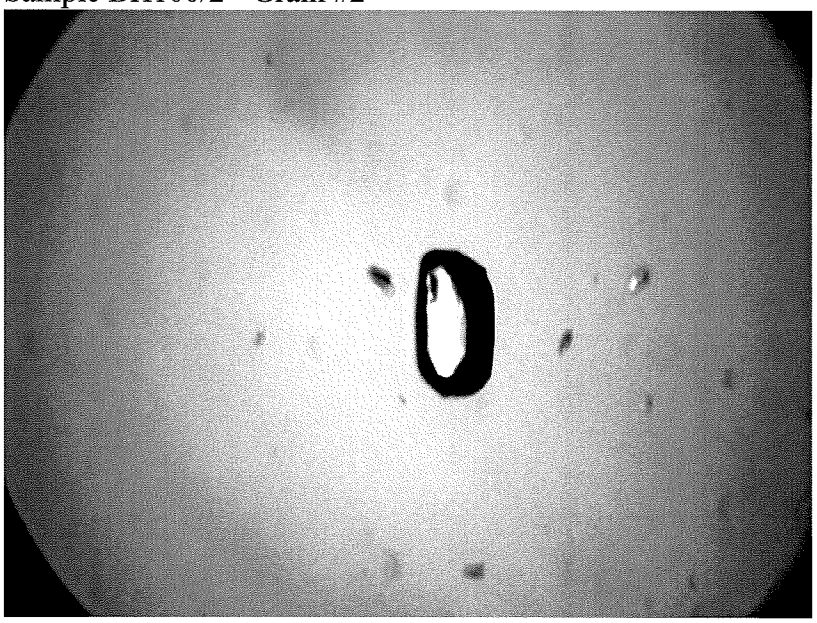

X-axis (Vertical): 260.4 μm
Y-axis (Horizontal): 144.6 μm

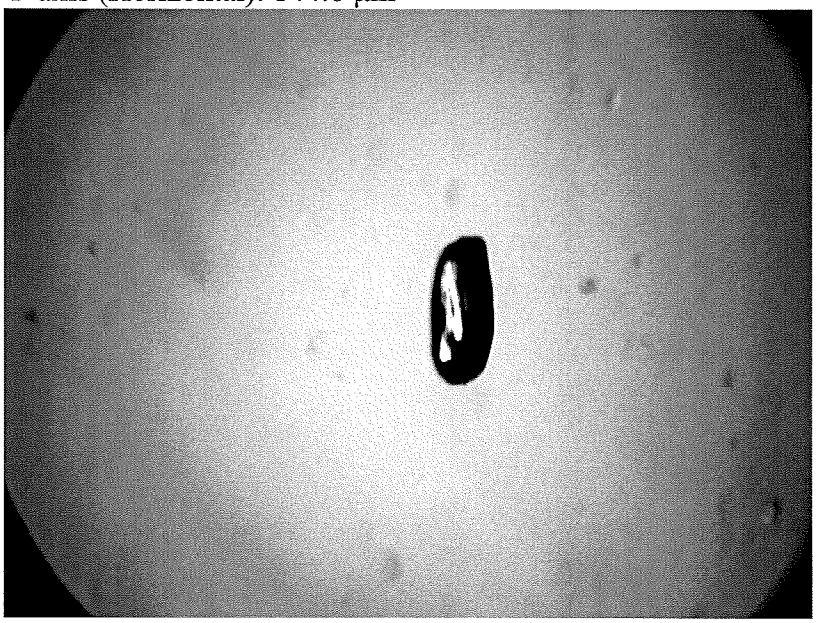

Z-axis (Horizontal): 112.1 μm

Description: Rounded grain, no obvious inclusions.

Sample BH100/2 - Grain #3

X-axis (Vertical): 224.2 μm
Y-axis (Horizontal): 141.1 μm

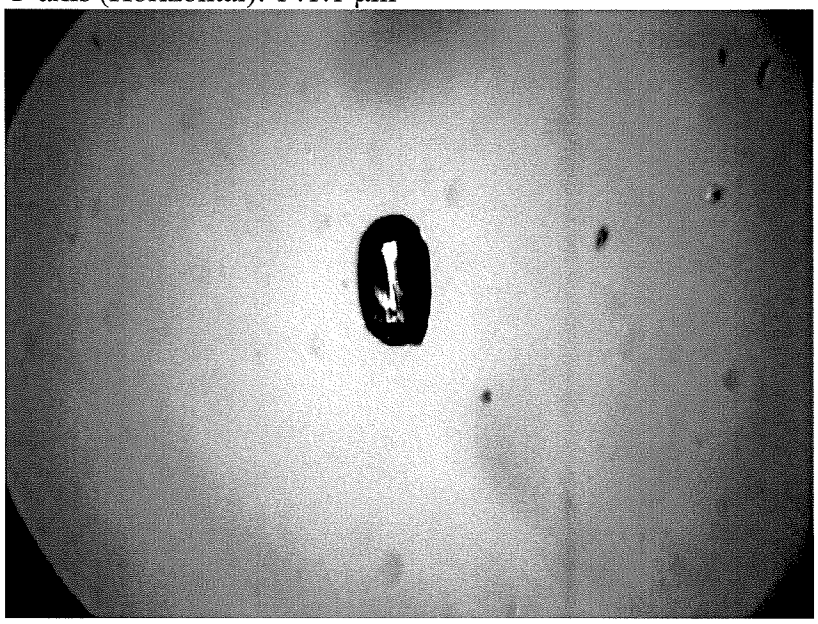

Z-axis (Horizontal): 128.4 μm

Description: Two small (1-5μm) fluid inclusions. Tabular shaped with one end broken off.

Sample BH100/2 - Grain #5

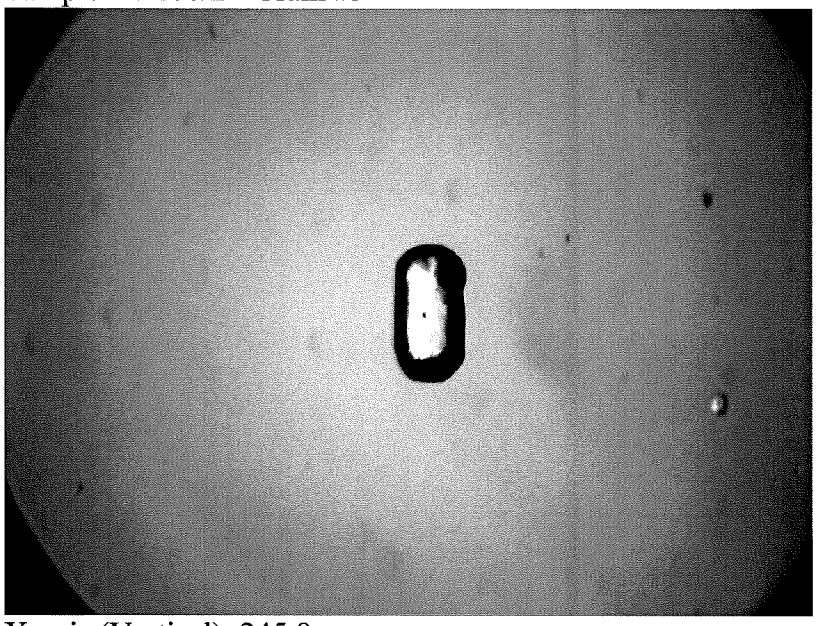

X-axis (Vertical): 245.9 μm
Y-axis (Horizontal): 124.7 μm

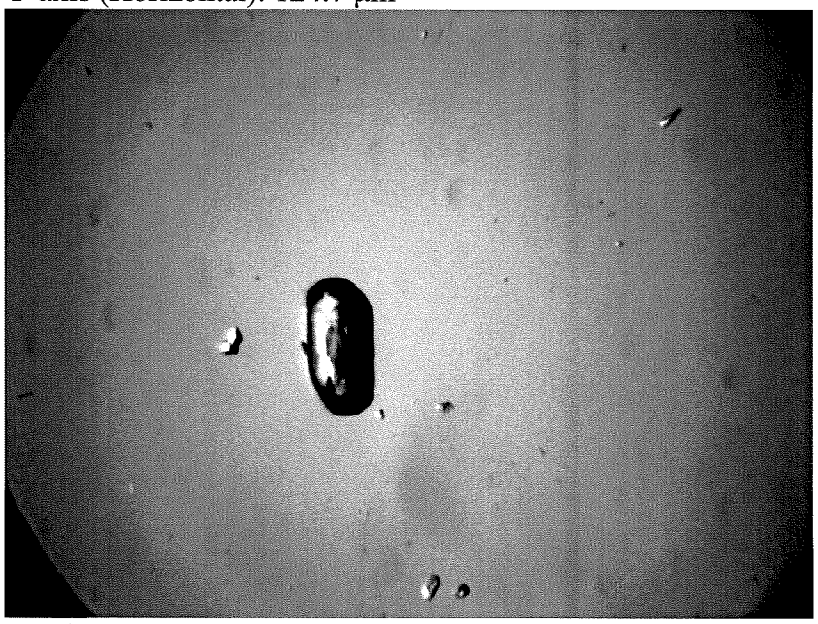

Z-axis (Horizontal): 115.7 μm

Description: One small (1-5μm) fluid inclusion. Both ends well rounded.

Sample BH101 - Grain #1

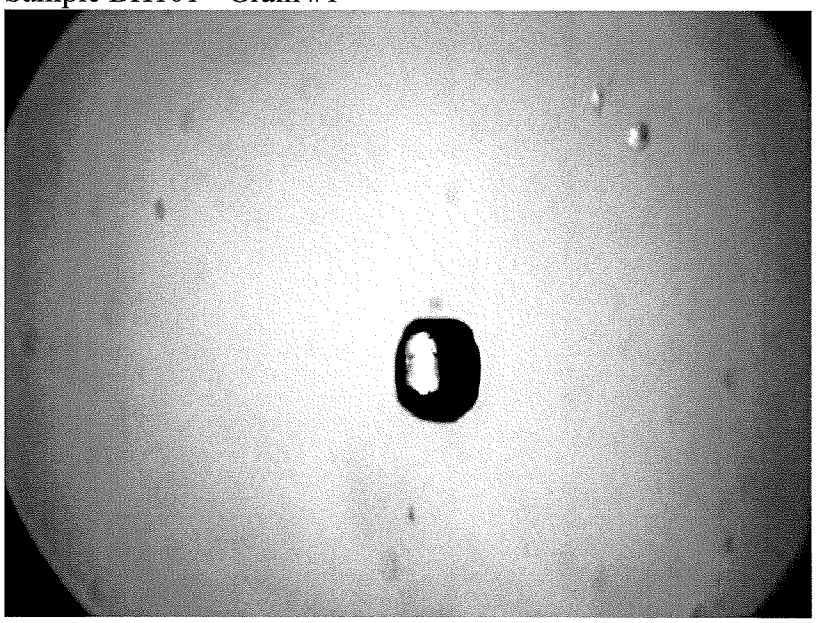

X-axis (Vertical): 184.4 μm
Y-axis (Horizontal): 151.7 μm

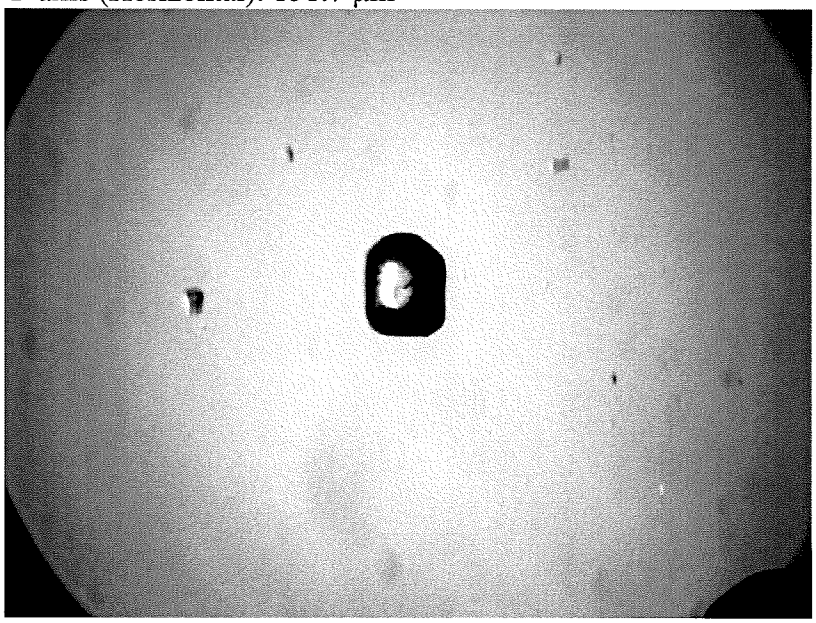

Z-axis (Horizontal): 137.4 μm

Description: Egg shaped crystal with 2 small (1-5μm) fluid inclusions.

Sample BH101 - Grain #2

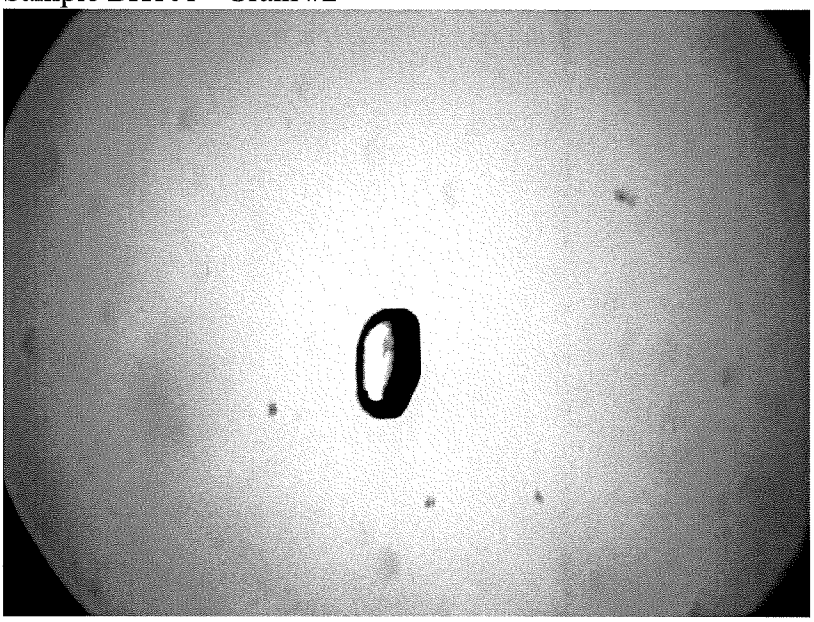

X-axis (Vertical): 195.2 μm
Y-axis (Horizontal): 113.9 μm

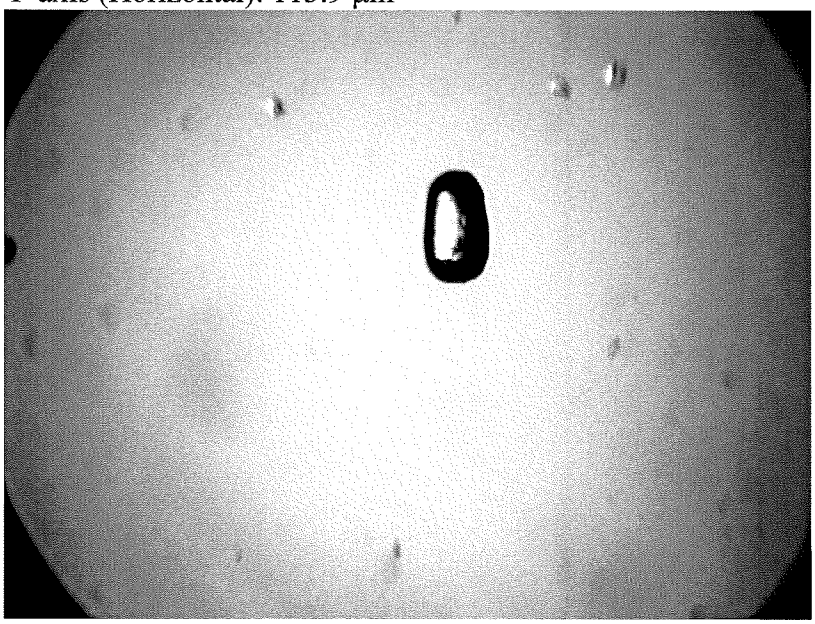

Z-axis (Horizontal): 112.7 μm

Description: Two well rounded edges with one 1-5μm long unknown mineral inclusion.

Sample BH101 - Grain #4

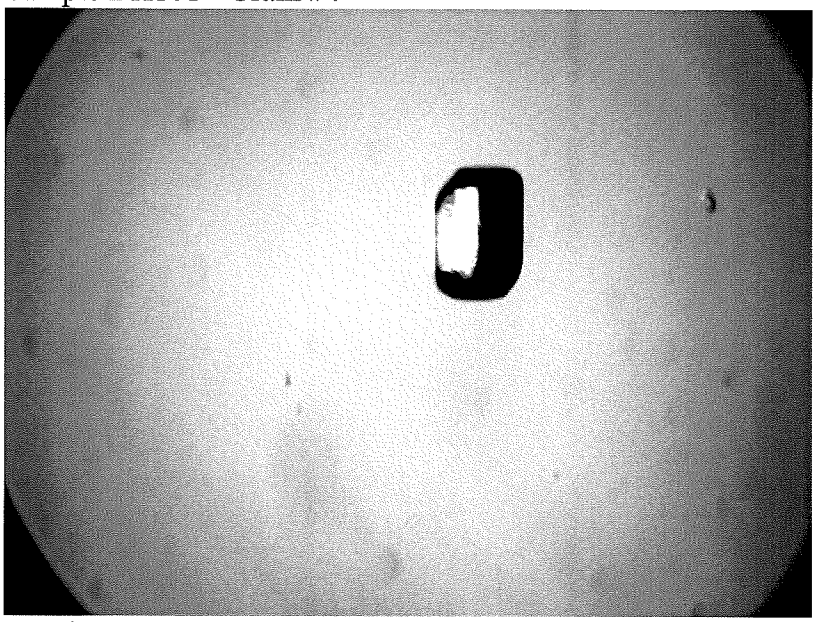

X-axis (Vertical): 235.1 μm
Y-axis (Horizontal): 159.2 μm

Z-axis (Vertical): 103.9 μm

Description: Both ends rounded with one end broken on the side. One small fluid inclusion (1-5μm) and 2 small patches of disseminated opaque mineral inclusions.

Sample BH101 - Grain #5

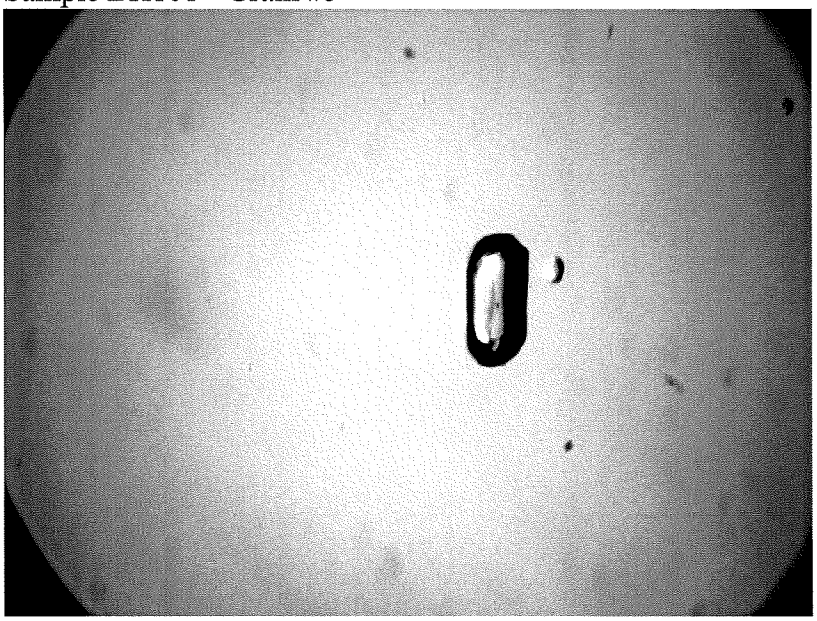

X-axis (Vertical): 236.8 μm
Y-axis (Horizontal): 106.7 μm

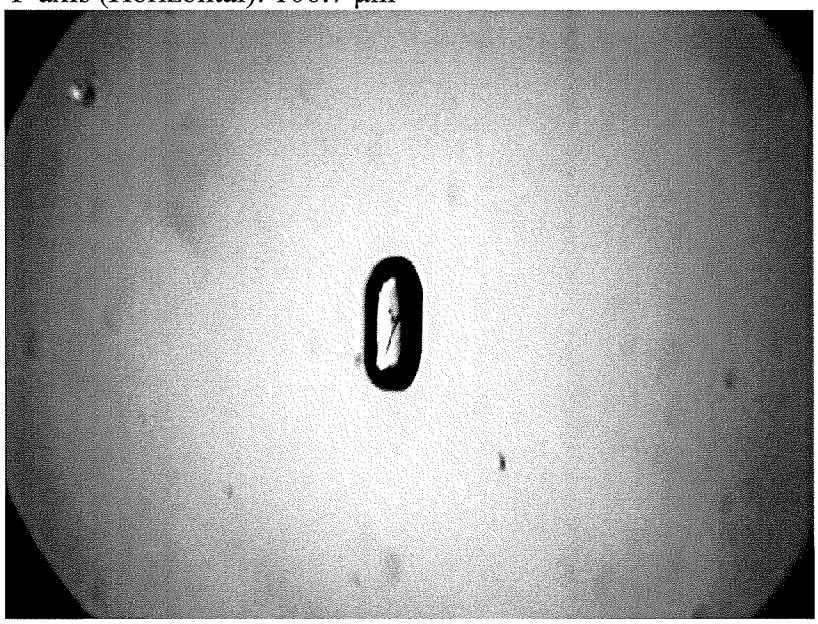

Z-axis (Horizontal): 103.1 μm

Description: One small (1-5μm) fluid inclusion and a possible surface crack. The crack does not penetrate deeply into the body of the grain.

Sample BH103 - Grain #1

X-axis (Vertical):164.5 μm
Y-axis (Horizontal): 88.7 μm

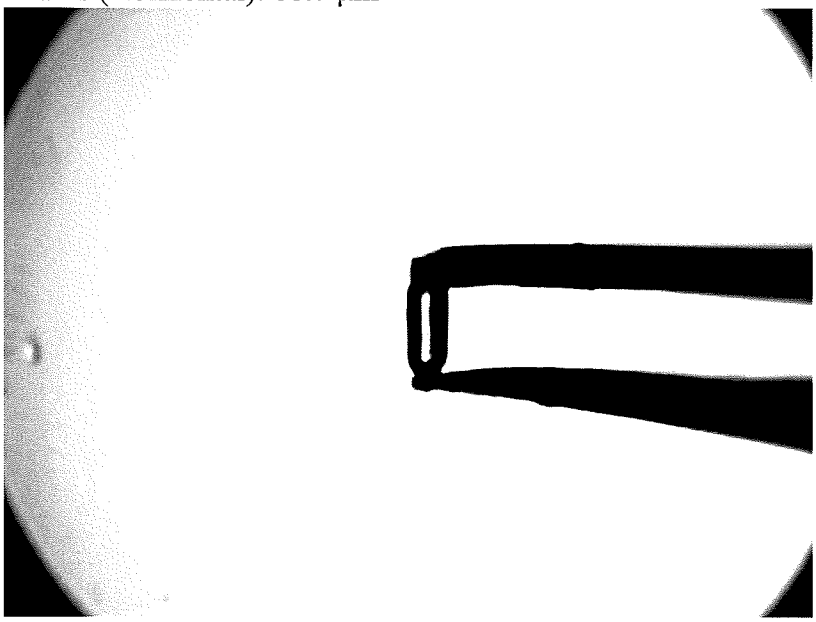

Z-axis (Horizontal): 77.7 μm

Description: One rounded end and one end broken off. Three small (1-5μm) fluid inclusions.

Sample BH103 - Grain #2

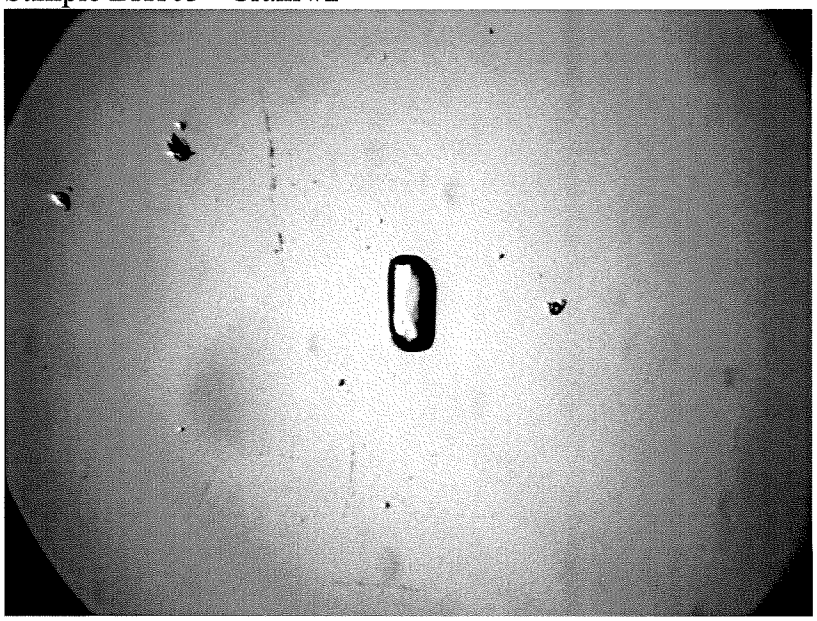

X-axis (Vertical): 171.7 μm
Y-axis (Horizontal): 88.6 μm

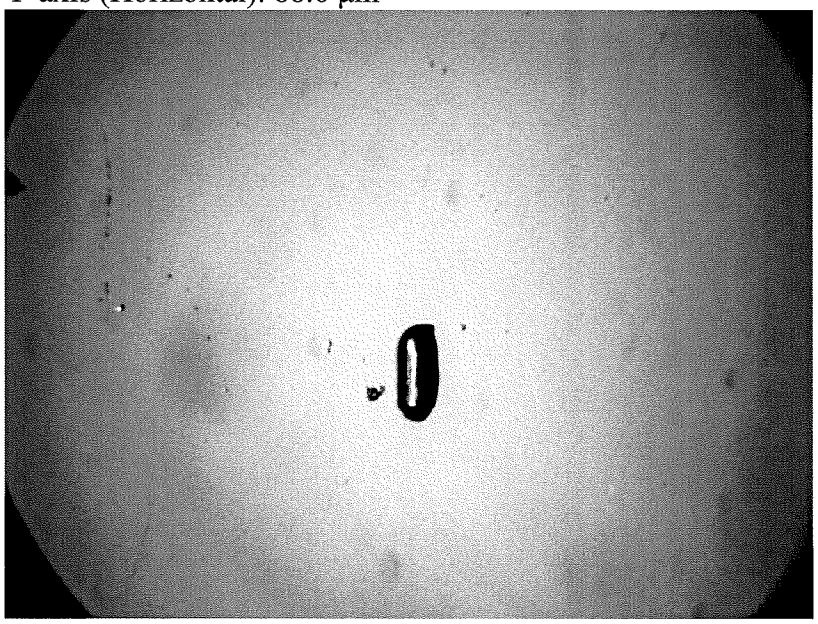

Z-axis (Horizontal): 75.9 μm

Description: Both ends rounded. Two small (1-5μm) fluid inclusions and four opaque mineral inclusions (<1μm).

Sample BH103 - Grain #3

X-axis (Vertical): 179.2 μm
Y-axis (Horizontal): 94.3 μm

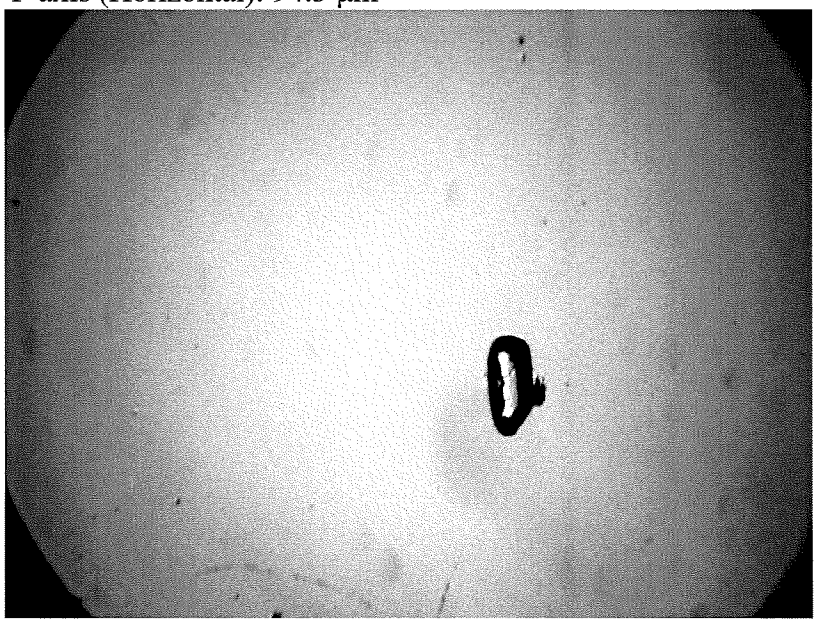

Z-axis (Horizontal): 83.3 μm

Description: One rounded end. No inclusions but surface is abraded.

Sample BH103 - Grain #4

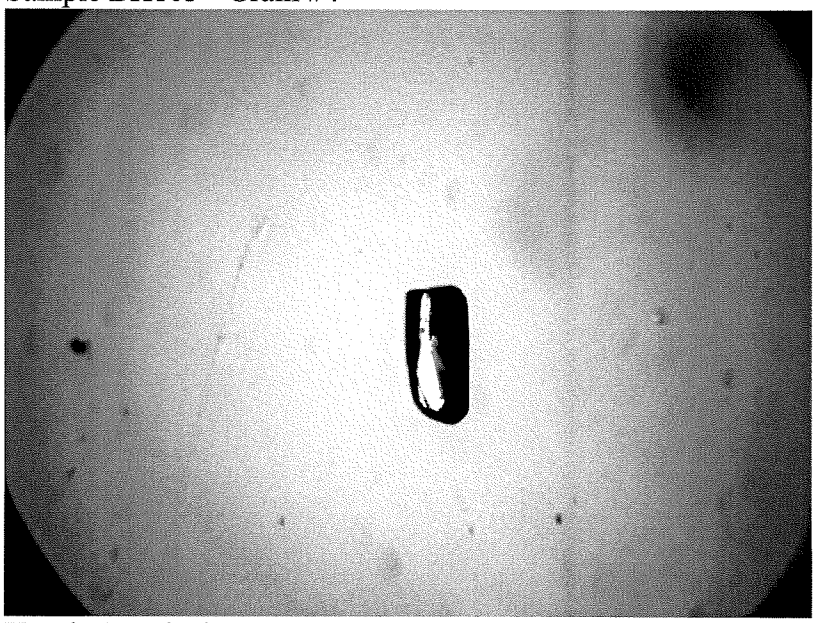

X-axis (Vertical): 231.5 μm
Y-axis (Horizontal): 110.3 μm

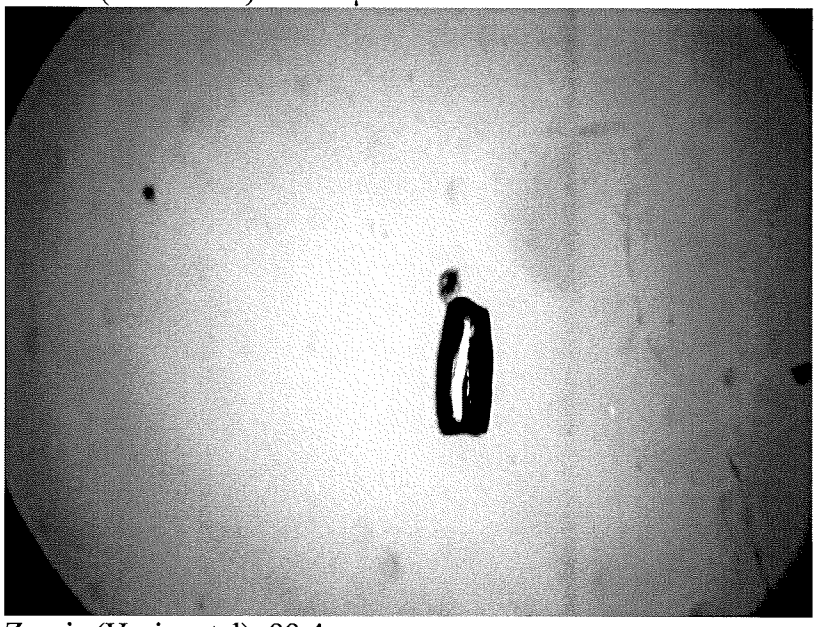

Z-axis (Horizontal): 99.4 μm

Description: One small (1-5μm) fluid inclusion. Irregular broken ends.

Sample BH104 - Grain #1

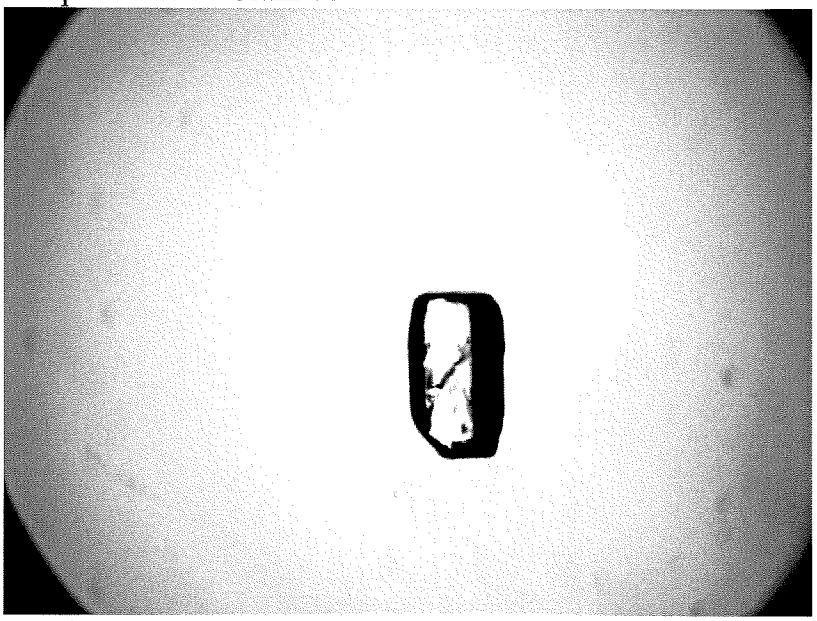

X-axis (Vertical): 296.5 μm
Y-axis (Horizontal): 171.8 μm

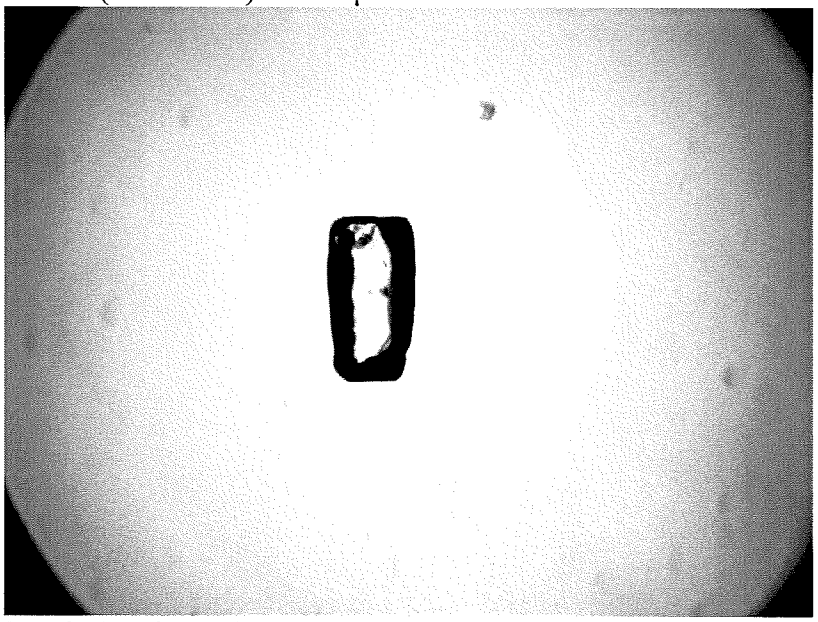

Z-axis (Horizontal): 153.7 μm

Description: Both ends flat and broken off. One small fluid mineral inclusion and one small fluid inclusion (both 1-5μm).

Sample BH104 - Grain #2

X-axis (Vertical): 229.6 μm
Y-axis(Horizontal): 119.4 μm

Z-axis (Horizontal): 110.3 μm

Description: Ends are moderately chipped. Two small fluid inclusions (1-5μm)

Sample BH104 - Grain #4

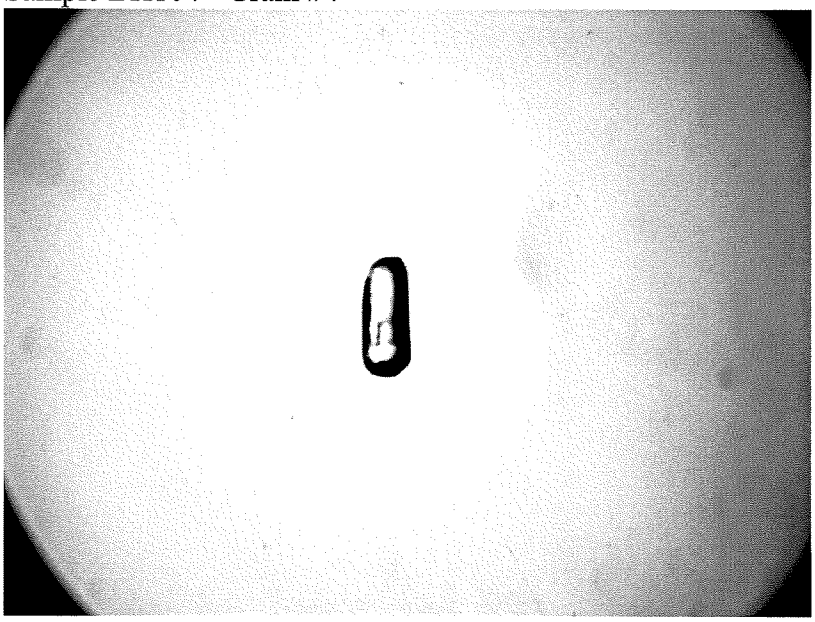

X-axis (Vertical): 211.5 μm
Y-axis (Horizontal): 88.2 μm

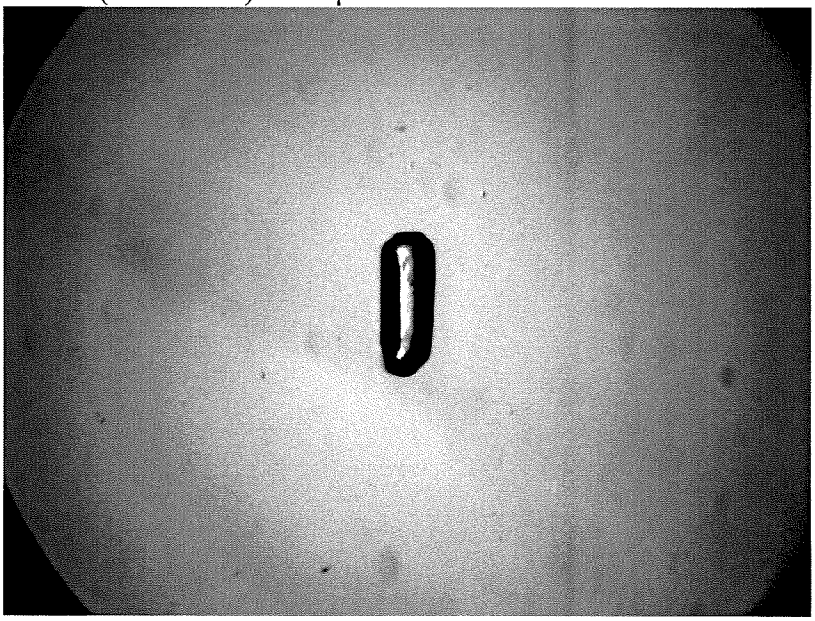

Z-axis (Horizontal): 95.8 μm
Description: Two surface cracks along the Y-axis of the grain and one small (1-5μm) fluid inclusion.

Sample BH104 - Grain #5

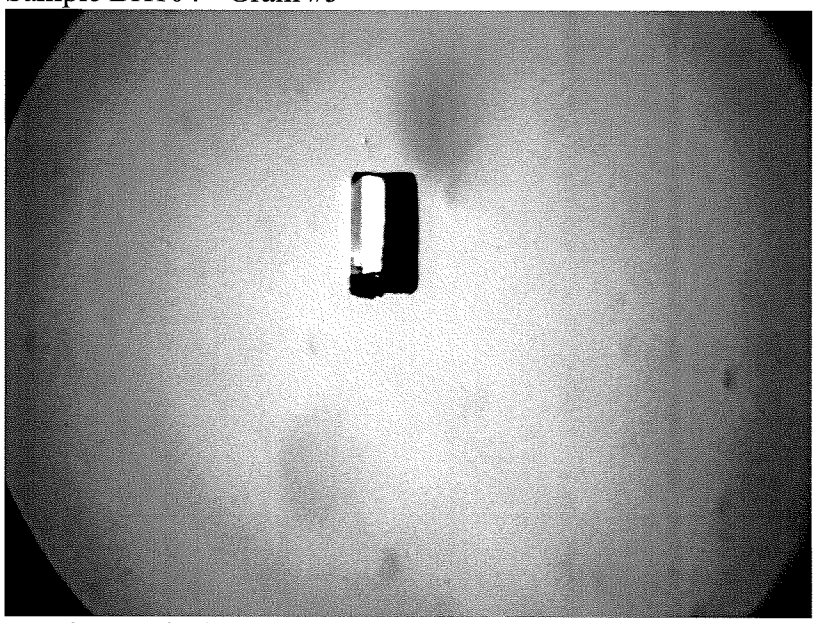

X-axis (Vertical): 218.8μm
Y-axis (Horizontal): 119.4 μm

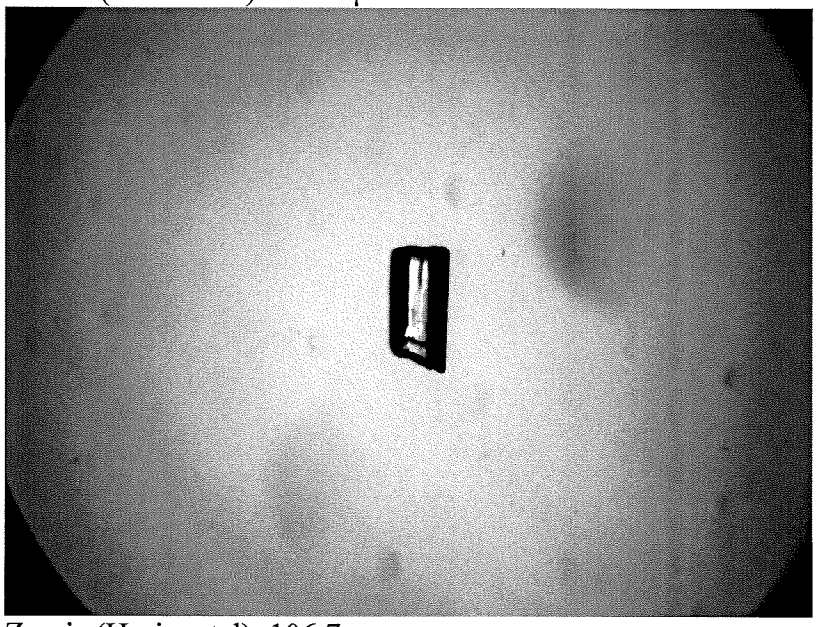

Z-axis (Horizontal): 106.7 μm

Description: Several 5-10μm needle-shaped inclusions and one 1-5μm fluid inclusion. Both ends are broken.

B. Appendix B – List of Tables

Table 1.1

Sample #	Sample Location		Elevation (m)
	Latitude (°N)	Longitude (°E)	
BH104	27.399139	90.996972	3710
BH103	27.399139	91.006333	3300
BH101	27.329000	91.055167	2300
BH100/2	27.308806	91.153889	1720

Table 3.1

Location	Sa. Name	4He(fmol)	Blk(fmol)	Blk.%	Re-ext.(fmol)	Re-ext.(%)	Lab no.
0							
1	BH104-1	8.26	0.52	6	0.06	0.69	299
2	BH104-2	3.29	0.53	13.86	0.015	0.46	300
3	BH104-4	2.34	0.52	18.09	0.189	8.07	301
4	BH104-5	1.60	0.52	23.70			302
5	BH103-1	2.14	0.56	20.78	0.156	7.21	304
6	BH103-2	1.38	0.57	29.32			303
7	BH103-3	2.20	0.56	20.20			305
8	BH103-4	2.74	0.54	16.36			306
9	PF1	not	analysed				
10	BH101-1	2.23	0.44	16.40	0.062	2.81	315
11	BH101-2	2.81	0.53	15.89	0.006	0.22	307
12	BH101-4	5.49	0.52	8.65	0.018	0.33	308
13	BH101-5	9.28	0.54	5.50			309
14	PF2	not	analysed				
15	BH100/2-1	0.03	0.52	94.45	0.027	70.49	310
16	BH100/2-2	0.01	0.54	97.78	0.021	127.84	311
17	BH100/2-3	0.07	0.55	88.20	0.002	2.81	312
18	BH100/2-5	-0.02	0.54	104.40			313
19	PF3	not	analysed				
20	DUR-7	72.23	0.49	0.67			316
21	DUR-8	76.56	0.48	0.62			317
22	DUR-9	36.81	0.47	1.27			318
23	DUR-10	lost					319

Table 3.1: From left to right, column titles: Sample name, concentration of ^{4}He in Fmoles (femtomole =10^{-15} moles), Bulk concentration in fmoles, Bulk % of concentration of ^{4}He, concentration of re-extracted ^{4}He in fmoles, re-extracted ^{4}He as % of original ^{4}He extraction, lab number. DUR samples represent the Durango apatite standards included in the measurements.

Table 3.2

concentration (ppt)				
sample	U238	Th232	Th/U	Sm147
ptbk1	1.46	8.15		0.30
ptbk1_r	1.29	11.27		0.21
ptbk2	1.97	10.34		0.08
ptbk3	1.62	10.83		0.32
BH100/2-1	-1.19	2.70	-2.26	-0.03
BH100/2-2				
BH100/2-3				
BH100/2-5				
BH101-1	70.12	13.42	0.19	61.44
BH101-2	37.56	7.90	0.21	46.75
BH101-4	137.06	38.76	0.28	88.25
BH101-5	219.35	70.30	0.32	66.57
BH103-1	24.25	10.90	0.45	4.94
BH103-2	39.26	11.41	0.29	4.05
BH103-3	39.38	7.80	0.20	8.12
BH103-4	80.91	-3.31	-0.04	8.74
BH104-1	173.35	105.32	0.61	23.22
BH104-2	72.26	36.66	0.51	36.25
BH104-4	60.99	32.60	0.53	4.82
BH104-5	44.19	0.97	0.02	9.41
dur7	60.10	95.75	1.59	24.32
dur7_r	63.94	116.98	1.83	42.66
dur8	69.03	747.10	10.82	149.20
dur9	27.75	635.75	22.91	50.21
bk1	0.03	0.15		-0.19
bk2	0.09	0.04		0.02

Table 3.2: Highlighted values show anomalous concentrations. Ptbk samples represent empty platinum tube blanks, bk samples represent non-platinum blanks. Grain BH100/2-1 was measured to test the theory that the entirety of sample BH100/2 had low parent isotope concentrations. BH100/2-2, 3 and 4 were not measured when this was confirmed after the first grain.

Table 3.3

samples	238U	232Th	147Sm	He	Raw Age	Age Error	Age Error	FT	Corrected	Age Error
	mol	mol	mol	mol	Ma	Ma	%		Ma	Ma
dur7	3E-13	5E-13	2E-13	7.2E-14	130.9276	3.549454	2.711005	1	130.9276	75.9409
dur8	4E-13	3.9E-12	1.2E-12	7.7E-14	46.82067	1.246874	2.663085	1	46.82067	32.72202
dur9	1E-13	3.4E-12	4.2E-13	3.7E-14	31.08647	0.905231	2.911978	1	31.08647	0.905231
bh10021				3E-17						
bh10022				1.2E-17						
bh10023				7.4E-17						
bh10025				-2E-17						
bh1011	4E-13	7.1E-14	5.1E-13	2.2E-15	4.534679	0.154731	3.412178	0.8072	5.617853	0.191691
bh1012	2E-13	4.2E-14	3.9E-13	2.8E-15	10.62676	0.369891	3.480755	0.7685	13.82879	0.481346
bh1014	7E-13	2.1E-13	7.3E-13	5.5E-15	5.612359	0.177921	3.17017	0.7993	7.022025	0.22261
bh1015	1E-12	3.7E-13	5.5E-13	9.3E-15	5.880345	0.183829	3.126153	0.7584	7.753821	0.242396
bh1031	1E-13	5.7E-14	4.1E-14	2.1E-15	12.07798	0.435007	3.601652	0.6957	17.36097	0.625282
bh1032	2E-13	6E-14	3.3E-14	1.4E-15	4.962923	0.182145	3.670108	0.6956	7.134304	0.261837
bh1033	2E-13	4.1E-14	6.7E-14	2.2E-15	8.027308	0.282378	3.517723	0.7158	11.21478	0.394505
bh1034	4E-13	-2E-14	7.2E-14	2.7E-15	5.156039	0.174935	3.392809	0.7603	6.781657	0.230089
bh1041	9E-13	5.5E-13	1.9E-13	8.3E-15	6.303667	0.190749	3.025995	0.8349	7.54992	0.22846
bh1042	4E-13	1.9E-13	3E-13	3.3E-15	6.118456	0.19118	3.124639	0.7738	7.907015	0.247066
bh1044	3E-13	1.7E-13	4E-14	2.3E-15	5.13536	0.166002	3.232525	0.7263	7.070667	0.228561
bh1045	2E-13	5.1E-15	7.8E-14	1.6E-15	5.428368	0.196788	3.625175	0.7727	7.025359	0.254682

Table 3.3: Highlighted values show age values that are outliers in the corrected age column. From left to right, column titles: Sample number, number of ^{238}U in moles, number of ^{232}Th in moles, number of ^{127}Sm in moles, concentration of ^{4}He in moles, raw age in years, raw age in millions of years, age error in millions of years, age error in % of raw age, α-particle ejection correction factor (Ft), corrected age of the samples in millions of years and age error in millions of years.

Table 3.4

	isotopic ratio U		**isotopic ratio Sm**	
sample	ratio238235	error %	ratio154152	error %
bh10021	15.67	-88.64	0.42	-50.78
bh10022	9.00	-93.47	0.50	-41.05
bh10023	7.44	-94.60	0.50	-41.21
bh10025	8.00	-94.20	0.50	-41.05
bh1011	168.73	22.37	0.86	0.73
bh1012	168.00	21.84	0.86	0.92
bh1014	139.00	0.81	0.86	1.03
bh1015	133.58	-3.12	0.86	0.79
bh1031	557.00	303.97	1.04	22.54
bh1032	279.33	102.59	1.11	30.07
bh1033	415.00	200.98	0.99	16.75
bh1034	198.67	44.09	0.99	16.85
bh1041	173.05	25.50	0.88	3.95
bh1042	260.83	89.17	0.85	0.10
bh1044	157.88	14.50	1.15	35.00
bh1045	336.67	144.17	0.93	9.50
dur7	790.00	472.96	0.84	-1.38
dur7_r	828.00	500.52	0.92	8.32
dur8	159.45	15.65	0.82	-3.46
dur9	174.80	26.78	0.85	0.35
bk1	0.5			
bk2	-1.3333333			

Table 3.4: Highlighted values show grains that have relatively high U or Sm values and that have ratios near the natural abundance. From left to right, column titles: ratio of ^{238}U to ^{235}U, % error of $^{238}U/^{235}U$ value, ratio of ^{154}Sm to ^{152}Sm, % error of $^{154}Sm/^{152}Sm$ value.

Table 3.5

Field code	Longitude	Latitude	Elevation	Number of grains	Spontaneous track density	Induced track density	Dosimeter	$P(\chi^2)$	Central age ± 1σ
BH100	91.563722	27.411389	0.905	21	1.203 (241)	43.357 (8686)	11.465 (8092)	75.2	5.9 ± 0.4
BH104	90.996972	27.399139	3.710	25	0.513 (123)	11.445 (2745)	10.399 (7383)	49.27	8.6 ± 0.8
BH103	91.006333	27.399139	3.300	24	0.672 (147)	16.748 (3663)	10.517 (7383)	77.35	7.8 ± 0.7
BH102	91.055167	27.329000	2.795	19	1.114 (148)	32.919 (4375)	10.428 (7383)	87.51	6.5 ± 0.6
BH101	91.100722	27.341333	2.380	39	0.42 (129)	13.106 (4022)	10.31 (7383)	90.36	6.1 ± 0.6
BH100/2	91.153889	27.308806	1.720	24	0.115 (26)	3.667 (829)	10.25 (7383)	97.47	5.9 ± 1.2

Table 3.5: AFT sample numbers, locations, elevations and ages along with other statistical values.